Near-Coastal Ultrahigh Resolution Scatterometer Winds

Nolan Hutchings

A thesis submitted to the faculty of
Brigham Young University
in partial fulfillment of the requirements for the degree of

Master of Science

David G. Long, Chair
Brian Jeffs
Cammy Peterson

Department of Electrical and Computer Engineering

Brigham Young University

ABSTRACT

Near-Coastal Ultrahigh Resolution Scatterometer Winds

Nolan Hutchings
Department of Electrical and Computer Engineering, BYU
Master of Science

RapidScat 2.5 km ultrahigh resolution (UHR) wind estimation is introduced and validated it in near-coastal regions. In addition, this thesis applies direction interval retrieval techniques and develops a new wind processing method to enhance the performance of RapidScat UHR wind estimation in the nadir region. The new algorithm is validated with L2B wind estimates, Numerical Weather Prediction (NWP) wind products, and buoy measurements. The wind processing improvements produce more spatially consistent UHR winds that compare well with the wind products mentioned above.

Hawaii regional climate model (HRCM), QuikSCAT, and ASCAT wind estimates are compared in the lee of the Big Island with the goal of understanding UHR scatterometer wind retrieval capabilities in this area. L2B scatterometer wind estimates do not resolve well the wind features shown in HRCM winds. UHR wind vectors better resolve fine resolution wind speed features, but still do not resolve the expected wind direction features. A comparison of scatterometer measured σ^0 and predicted HRCM and NWP σ^0 suggests that scatterometers can detect a reverse flow in the lee of the island. Differences between scatterometer measured σ^0 and HRCM predicted σ^0 indicate error in the placement of key reverse flow features by the model. Coarse nudging fields and a large fixed size median filter window are also shown to impede UHR wind retrieval in this area.

ACKNOWLEDGMENTS

TABLE OF CONTENTS

LIST OF FIGURES

CHAPTER 1.   INTRODUCTION

1.1   Overview

Satellite radar instruments called "scatterometers" illuminate the Earth's surface with microwaves and measure the normalized radar cross-section (σ^0) [1]. From scatterometer ocean σ^0 measurements and wind models, estimates of wind speed and direction can be made over the open ocean. Unlike wind measurements from buoys, ships, planes or other sensors, scatterometers provide regular global wind vector estimates over large regions of open ocean. The large coverage and availability of scatterometer data proves useful for many applications [1, 3–6]. These estimates are excellent for understanding large scale wind flow and other features. Traditional wind estimates are retrieved on a coarse 12.5 or 25 km grid. Wind estimates close to shore are discarded due to land contamination of ocean σ^0.

The Microwave Earth Remote Sensing Lab at Brigham Young University produces wind estimates for multiple sensors on an ultrahigh resolution (UHR) 2.5 km or 1.25 km grid. UHR wind processing reveals finer resolution detail of ocean wind phenomena and gives us valuable insight to complex close to shore wind phenomena [7–10]. Finer resolution wind products allow wind estimation closer to shore, but they still suffer from land contamination. A new technique called land contamination removal ameliorates this problem and allows UHR wind estimation closer to shore than ever before [9]. UHR wind products are produced for RapidScat, QuikSCAT, and ASCAT scatterometers.

RapidScat is a dual pencil-beam Ku-band (13.4 GHz) scatterometer that operated on the International Space Station (ISS) from October 2014 to August 2016 [11]. RapidScat's mounting on the ISS presents some complications for wind estimation. For antenna azimuth angles 70°–116°, the RapidScat transmitter does not emit in order to avoid exposing docked spacecraft to the transmitted signal [11]. This gap in emission is referred to as "sector blanking". Sector blanking produces fewer σ^0 measurements, which adversely affects wind estimation accuracy. Sector blank-

ing can also result in data gaps in the estimated wind field swath, as seen in Chapter 3 Fig. 3.10. Traditional 12.5 km RapidScat wind estimates have been validated with Numerical Weather Prediction (NWP) winds and buoy measurements [11–13].

The SeaWinds instrument on QuikSCAT (referred to as QuikSCAT) launched in June of 1999. QuikSCAT had a long mission life of 10 years that ended due to mechanical failure. The long continuous data collected makes QuikSCAT a great calibration and comparison tool for other scatterometers. Like RapidScat, QuikSCAT is a Ku-band dual pencil-beam scatterometer [14]. Coarse QuikSCAT wind products and UHR wind products have both been validated [8, 15, 16].

ASCAT (short for Advanced scatterometer) launched in 2007 aboard MetOp-A and is still collecting data to date [17]. ASCAT differs from the previously two mentioned scatterometers in that it is a fan-beam scatterometer and it operates a C-band (5.255 GHz) [18]. Coarse ASCAT wind products and UHR wind products have both been validated [9, 19].

1.2 Thesis Statement

While wind scatterometry has advanced considerably in recent years, there is still much work to be done to improve near coastal UHR wind estimation. This thesis focuses on UHR wind estimation in two near coastal areas from multiple sensors. First, near-coastal RapidScat UHR wind estimates near the east coast of the United States are introduced and validated. Then, new algorithms are applied to improve RapidScat UHR wind retrieval in that area. Second, near Hawaii, QuikSCAT and ASCAT UHR wind estimates are compared to near-Hawaii model winds and UHR capabilities in this region are detailed.

1.3 Summary of Results

Conventional RapidScat UHR wind estimates are first shown to be reasonable estimates of wind speed and direction in near-coastal areas. Then, a wind retrieval algorithm that has been applied previously to other scatterometers is applied to RapidScat UHR wind retrieval. The algorithm improves wind estimation in near coastal areas. A new algorithm is also applied to RapidScat wind retrieval to further improve the accuracy of UHR wind estimates in the near-nadir region of the swath.

QuikSCAT and ASCAT UHR wind estimates are compared with high resolution model winds near Hawaii. The comparison shows that scatterometers do not resolve all of the features included in the model. The wind speed features are resolved well, but the complex wind direction features appear to be absent in the final selected wind field. A comparison of measured scatterometer σ^0 and model simulated σ^0 indicates some error in the models placement of certain wind features. The results also suggest that the scatterometers are detecting the reverse flow. Finally, coarse nudging fields and a relatively large fixed size median filter are shown to hinder wind retrieval of small scale features. Further advances in scatterometry and a better representation of fine scale features near Hawaii is needed to improve UHR wind retrieval.

1.4 Outline

Chapter 2 provides necessary background information on scatterometers. Different scatterometer architectures and details on wind retrieval and ambiguity selection are explained. Chapter 3 first validates near-coastal RapidSCAT UHR wind estimates near the east coast of the United States. Then, direction interval retrieval is applied to the RapidScat UHR wind processing algorithm along with a new technique to improve near nadir wind estimation. UHR estimates processed with the new algorithm are validated in the same region. Chapter 4 explores QuikSCAT and AS-CAT UHR wind estimates near Hawaii. UHR estimates from both sensors are compared to high resolution model winds vectors to better understand UHR capabilities in this region. Model predicted σ^0 are also compared with scatterometer measured σ^0. The effects of nudging fields and median filter window size on UHR wind fields are also discussed. Finally, Chapter 5 concludes and presents contributions and ideas for future work.

CHAPTER 2.   BACKGROUND

This chapter provides background for the rest of the thesis. It describes the two main scatterometer architectures. Details of scatterometer wind estimation are discussed including generation of ambiguous wind vector solutions from σ^0 and a geophysical model function. Selection of a unique wind field and spatial filtering techniques are then considered. This chapter concludes with a discussion of difficulties and short comings of conventional scatterometer wind estimation.

2.1   Scatterometers

Scatterometers are active microwave sensors that estimate wind speed and direction over the open ocean by measuring the normalized radar cross section (σ^0) from a wind-roughened ocean surface. Wind vector data from scatterometers are used in a variety of oceanic studies and in weather forecasting [1, 3].

The two main architectures for scatterometers are pencil-beam and fan-beam scatterometers. QuikSCAT and RapidScat are examples of pencil-beam scatterometers, see Figs. 2.1 and 2.2. Pencil-beam scatterometers measure σ^0 as their inner and outer beams trace a helical pattern directly below the satellite on the surface. This pattern allows measurement of σ^0 from multiple azimuth and/or incidence angles at a single location.

ASCAT is a scatterometer with a fan-beam architecture and measures σ^0 from six stationary antennas (three on each side of the satellite) each placed at different azimuth angles, see Fig. 2.1 [18]. The fan-beams cover a wide swath on both sides of the satellite with a nadir gap directly below the satellite where no measurements are made.

2.2   Scatterometer Wind Estimation

To enable wind retrieval over the ocean, σ^0 measurements are collected at multiple azimuth/incidence angles ("looks") at each swath resolution element (wind vector cell, WVC). Wind
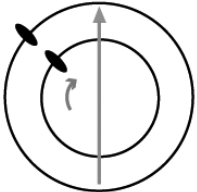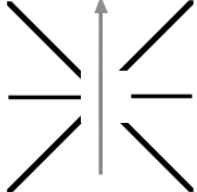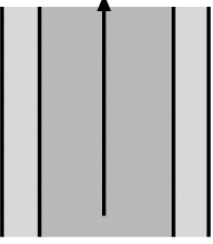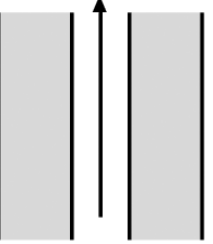
	SeaWinds	**ASCAT**
Frequency & Band	13.4 GHz (Ku)	5.3 GHz (C)
Antenna Configuration		
Polarization	VV-outer / HH-inner	VV
Beam Resolution	Pencil-beam	Range gate
Resolution ($\sigma°$)	Egg: 25x35 km Slice: 6x25 km	SZO: 25/50 km SZF: 4x20 km
Swath Configuration & Width in km	1400,1800	500 500
Incidence Angles	46° & 54.4°	25° - 65°
Mission & Dates	QuikSCAT: 6/99-11/09* ADEOS-II: 1/02-10/02 RapidScat: 10/14-8/16	METOP-A: 6/07- METOP-B: 9/12-

Figure 2.1: Pencil-beam (first column) and fan-beam (second column) scatterometer swath geometry and other important parameters. Figure is modified from [1].

retrieval requires diverse σ^0 measurements to solve for both wind speed and direction. Scatterometers obtain multiple look angles via rotating pencil-beam antennas (Fig. 2.2 or multiple stationary fan-beam antennas. Each approach results in several (2–4) backscatter measurements (sometimes called "flavors") at different azimuth and/or incidence angles for each WVC [14].

Wind retrieval uses a geophysical model function (GMF) to relate the σ^0 measurements in each WVC to 10 meter equivalent neutral wind vectors [20]. The GMF is an empirically derived

relationship (G) between σ^0 and wind and scatterometer parameters that can be written as: [1]

$$\sigma^0_{gmf} = G(|S|, \chi, \cdots; \theta, f, \text{pol}),$$ (2.1)

where S is the wind speed, χ is the difference between the azimuth look angle of the antenna and the wind direction (ϕ), θ is the beam incidence angle, f is the frequency of the beam, and pol is the polarization of the beam, and "$\cdots$" are other possible wind parameters which are not accounted for.

Because σ^0 measurements are noisy, a likelihood objective function $f(S, \phi)$, is formulated for S and ϕ for each WVC using the measured σ^0 (σ_{0i}), noise variance parameters (sd$_i$) [21], and the GMF evaluated at S, ϕ, (σ'_{0i})

$$f(S, \phi) = -\sum_i \left(\frac{\sigma_{0i} - \sigma'_{0i}(S, \phi)}{\text{sd}_i} \right)^2.$$ (2.2)

The multiple local maxima of the objective function lead to several possible solutions [22].

Each wind speed and direction pair associated with the objective function's local maxima is referred to as an "ambiguity". There are up to four ambiguities for each WVC. The ambiguities have similar wind speeds, but different wind directions. Selection of a unique estimate, a process called "ambiguity selection", begins by creating an initial wind field of estimates by "nudging" the grid of ambiguous solutions with another wind product (e.g., NWP winds for RapidScat L2B), which is referred to as the "nudging field". For each WVC in the swath, the nudging process selects the ambiguity that is closest in direction to the corresponding wind from the nudging field [21]. The resulting wind field is referred to as the "nudged field".

The nudged wind field is then iteratively updated using a median filter-based ambiguity selection scheme to produce a more spatially consistent final wind vector field [21, 23, 24]. For each WVC, the median filter-based ambiguity selection scheme compares the directions of its ambiguities with the directions of the selected ambiguities of the surrounding WVCs contained in the filter window. The ambiguity of the center WVC that is the direction closest to the circular median direction of the window is chosen to replace the current ambiguity choice for the center WVC. The median filter-based ambiguity selection scheme iterates until a pass through the whole

swath is completed without any ambiguity choices being changed or until the maximum number of iterations is reached [23].

Ambiguity selection in scatterometer wind processing has historically proven to be difficult and prone to error. Ambiguity selection is especially difficult in the nadir and far-swath regions for pencil-beam scatterometers [21]. Due to a limited azimuth angle diversity in these regions, the wind retrieval process can generate inaccurate solutions for ambiguity selection. In particular, the azimuth angles of fore and aft looks in the nadir region are almost 180° apart, see Fig. 2.2(a). In the far-swath region there are only measurements from the outer beam, and they have similar azimuth angles, see Fig. 2.2(c). For comparison, Fig. 2.2(b) shows the beam orientations of optimal "sweet spot" looks. Adverse weather conditions can also result in poor wind retrieval (e.g., rain).
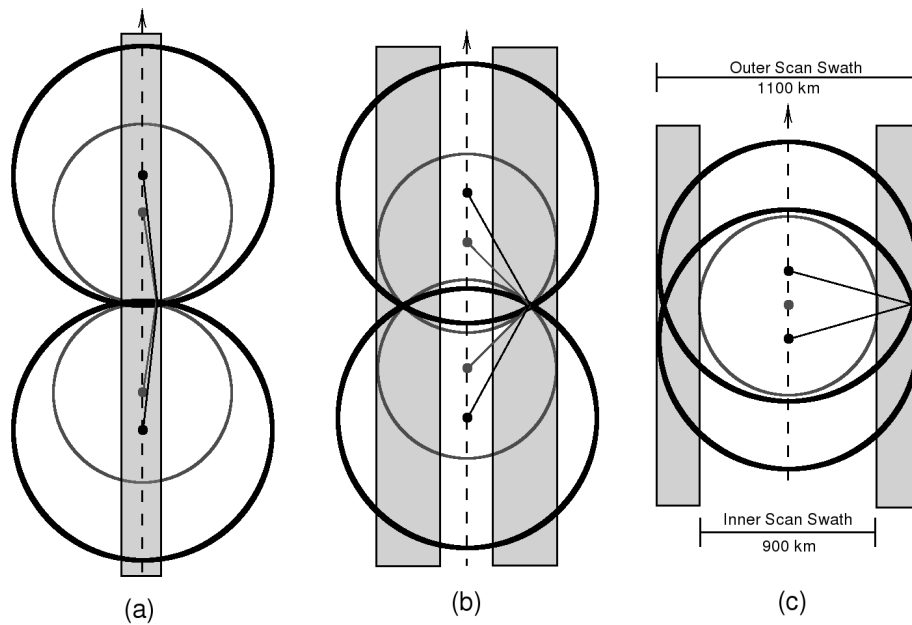
Figure 2.2: Illustrations of beam orientations for nadir (a), "sweet spot" (b), and far-swath (c) looks. The dashed lines show the nadir satellite path. The bold dots along the dashed lines are satellite positions in the swath at different times. The lines extending from the dots show the azimuth angles of the beams for a particular WVC. The smaller circles represent the inner-beam's reach and the larger circles represent the outer-beam's reach. The shaded boxes contain WVCs that have similar quality azimuth looks as the ones depicted. Note that for (a) there are effectively only two azimuth angles, while for (c) there is effectively only a single azimuth angle. In (b) there are four azimuth angles.

8

A complication for both pencil-beam and fan-beam scatterometers is land contamination. Land contamination refers to the effects of the higher reflectivity of the land in comparison to the water. Antenna side lobes can allow strong land echos to "contaminate" the lower ocean σ^0 measurements, which leads to erroneous wind speed values in near coastal regions. Previously, land contamination was avoided by discarding wind estimates that fall within 30 km of land. However, wind estimates closer to the coast can be retrieved with the spatial response function and a binary land map, which are used to calculate the land contamination ratio (LCR) [9]. For each σ^0 measurement, an LCR is computed and thresholded to decide if the σ^0 measurement is contaminated by land. Using only uncontaminated σ^0 measurements enables accurate wind retrieval [9].

Despite these complications, scatterometers have been a reliable source of wind vector data since 1970. Estimates from many sensors have been well validated and continue to contribute to the growing scatterometer wind vector data base. Improvements in wind estimation are constantly being made, even on decommissioned sensors. Wind vector estimates have been improved with high quality GMFs and new wind retrieval techniques.

CHAPTER 3. IMPROVED ULTRA HIGH RESOLUTION WIND RETRIEVAL FOR RAPIDSCAT

UHR wind estimation is not unique to RapidScat and has previously been applied in AS-CAT and QuikSCAT wind estimation [7–9]. As described earlier, UHR estimates can potentially estimate wind features closer to shore and reveal finer resolution wind phenomena. I choose to validate RapidScat UHR estimates in a near-coastal region off the East Coast of the United States due to the large number of buoys available for collocation. In addition, RapidScat UHR estimates are compared with L2B estimates.

3.1 Validation of Near-Coastal UHR Wind Estimates

Near-coastal RapidScat UHR wind estimates with LCR are validated by collocating UHR wind vectors with offshore buoy measurements and L2B estimates. A collocated UHR estimate is the UHR wind vector located closest to the buoy (within 2.5 km) and collected within 30 minutes of the buoy measurement. L2B collocations are within 12.5 km and 30 minutes of the buoy measurement. Buoy data are taken from the National Data Buoy Center (NDBC) [2]. Because of varying anemometer heights among the buoys, the buoy measurements are converted to represent 10 meter equivalent neutral wind vectors to match the reported scatterometer data [20]. Buoys provide an 8 minute temporally averaged measurement of wind speed and direction.

UHR estimates are averaged over a 5 x 5 WVC window (same area as a single L2B WVC) around the center collocated UHR WVC for comparison with the low resolution L2B estimates. The same averaging approach is used for comparison with buoy measurements. The UHR ambiguities averaged in the window are the ambiguities of each WVC with the direction closest to the reported buoy direction (this choice of ambiguity is referred to as C2B, closest to buoy). The C2B ambiguity represents the best case scenario for the ambiguity selection.

11

The buoys used in this study are located on the southeast coast of the United States (see Fig. 3.1) and satisfy the same criteria as in [25]: only moored sea buoys that have data necessary for U10 conversion, air and sea surface temperatures, surface pressure and near surface relative humidity, are used. Buoy measurements are treated as "true" values in this study. For more regarding buoys-based validation, see [25].
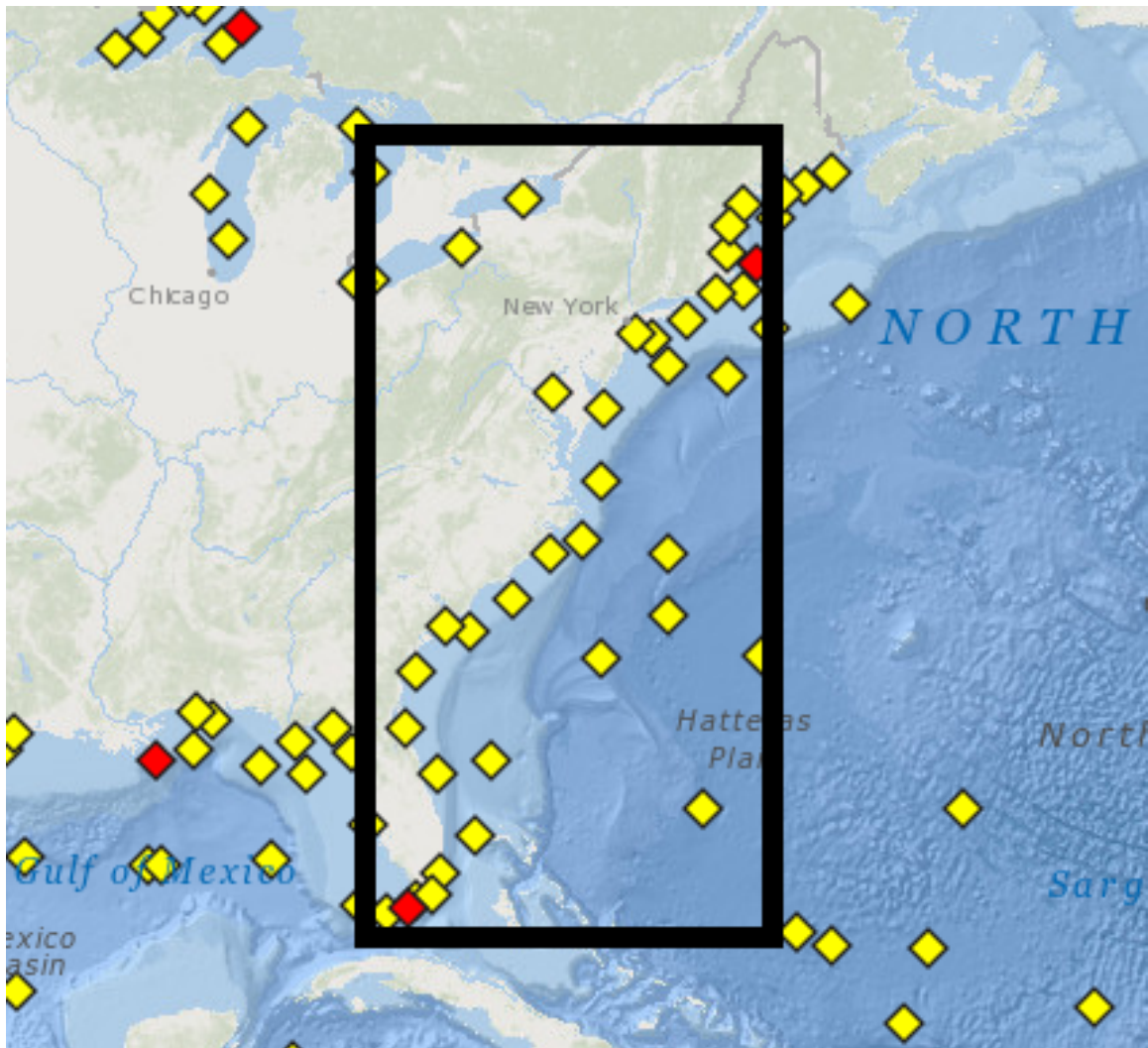
Figure 3.1: Buoy locations from NDBC and the approximate region used in this study. Latitude 25° to 45° N and Longitude 70° to 82° W. Figure modified from [2].

A year's worth of RapidScat wind estimates, taken from August 2015 through August 2016, are collocated with buoys. A total of 4856 buoy collocations are found in the study region shown in Fig. 3.1.

In August 2015, RapidScat experienced a 10 dB increase in noise [11]. The increase in noise level was not constant and varied between low and high noise states. The high noise state was prevalent for most of the mission after the problem arose. The increase in noise results in degraded wind speed estimation. Of the original 1154 orbits in which collocations occur, 81 are deemed poor or marginal quality due to high noise and are subsequently removed from the study, resulting in the number of collocations stated above. Section 3.1 discusses the wind speed comparison between C2B UHR (hereafter referred to as UHRB), L2B, and buoy measurements. Section 3.1 is an analysis of the UHRB wind direction.

UHRB Wind Speed Accuracy

I first consider wind speed. In Fig. 3.2, UHRB (b) and L2B (a) wind speed estimates are plotted against buoy wind speed measurements. The plots reveal that the L2B estimates match the buoys over a wide range of wind speeds. However, UHR processing overestimates low wind speeds and the UHRB estimates are noisier than the L2B wind vectors for most wind speeds. For moderate wind speeds (7 m/s to 15 m/s), UHRB has similar results as that of the L2B wind speed estimates. Due to the limited number of observations it is difficult to draw conclusions on high wind speed estimates.

In Fig. 3.3, the collocated UHRB and L2B wind speeds are averaged within 0.5 m/s buoy wind speed bins and the percentage difference from the mean buoy wind speeds is shown. Consistent with Fig. 3.2, at low wind speeds the UHRB estimates exhibit greater difference than L2B compared to the buoy measurements. The plot shows that for wind speeds over 7 m/s and below 18 m/s the UHRB estimates are on average within 10% of buoy measurements. This is within the accepted accuracy requirements given in [25], i.e., that estimates are within 10% or 1 m/s of buoy measurements. Fig. 3.4 presents a comparison of mean UHRB and L2B wind speeds with standard deviation lines. Remarkably, the standard deviation for both UHRB and L2B are similar for all wind speeds. However, for low wind speeds, the UHRB estimates are biased high, which is consistent with higher noise in the estimates [25]. The plot shows the same trends for low, middle, and high wind speeds as the previously mentioned plots.
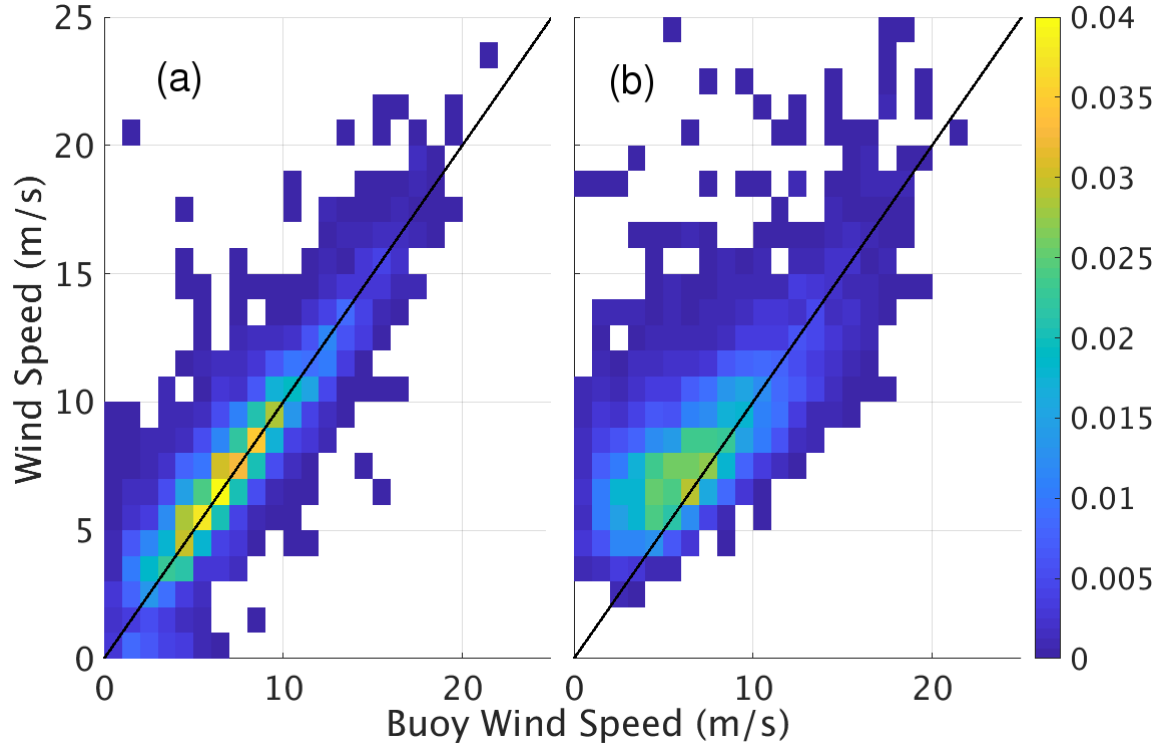
Figure 3.2: Scatter density plots of L2B (a) and UHRB (b) wind speeds plotted with collocated buoy wind speed measurements. A $y = x$ (solid line) is included for reference. UHRB wind speed estimates are noisier and biased higher, especially at low wind speeds.

UHRB Wind Direction Accuracy

Wind directions are now considered. Fig. 3.5 presents L2B (a)–(c) and UHRB (d)–(f) wind directions with collocated buoy measurements sorted by wind speed. The top row has collocations at all wind speeds, the middle row at wind speeds less than 7 m/s, and the bottom row at wind speeds greater than 7 m/s. As expected, the UHRB wind direction estimates are noisier than the L2B winds. However, the UHRB direction estimates tend to be more concentrated within $\pm 90°$ than the L2B winds at low wind speeds. Fig. 3.6 shows the L2B and UHRB circular mean and standard deviation of the angular difference from buoy measurements. Due to the circular nature of the direction angles, a circular mean must be computed, which is done as the multi-valued tangent inverse of the sum of the sine and cosine of the directions, as seen in Eq. 3.1 below:

$$\mu_c = \text{atan2}(\sum_{i=1}^{n} \sin(\theta_i), \sum_{i=1}^{n} \cos(\theta_i)) \qquad (3.1)$$

14
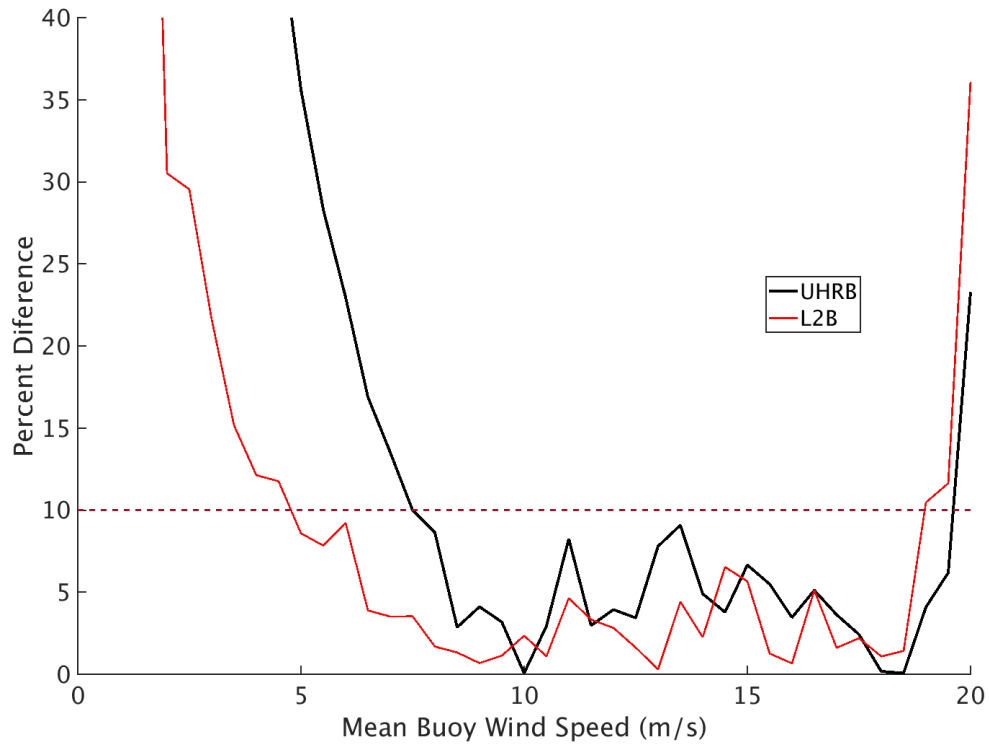
Figure 3.3: Percentage difference of mean L2B and mean UHRB estimates from mean buoy measurements. The horizontal dashed line shows the 10 percent difference boundary. Mean UHRB estimates exceed the boundary below 7 m/s, while mean L2B exceeds the boundary below 5 m/s. There are too few measurements at high wind speeds to draw any conclusions.

,where μ_c is the circular mean, n is the number of directions in a given bin, and θ_i is the direction. The circular means of both L2B and UHRB are consistent, i.e., they both closely follow the $y = x$ line. Further, the standard deviation of the UHRB estimates is similar to that of the L2B estimates. The low standard deviations near 0 (360) are puzzling, but are consistent with L2B estimates.

Summary of Near-Coastal UHRB Performance

Based on buoy comparisons, UHRB wind vectors are generally reliable despite being noisier than L2B estimates. At low wind speeds (< 7 m/s), the UHRB estimates are biased high. At higher wind speeds, UHRB wind speed estimates better match the buoy measurements than at lower speeds.

15
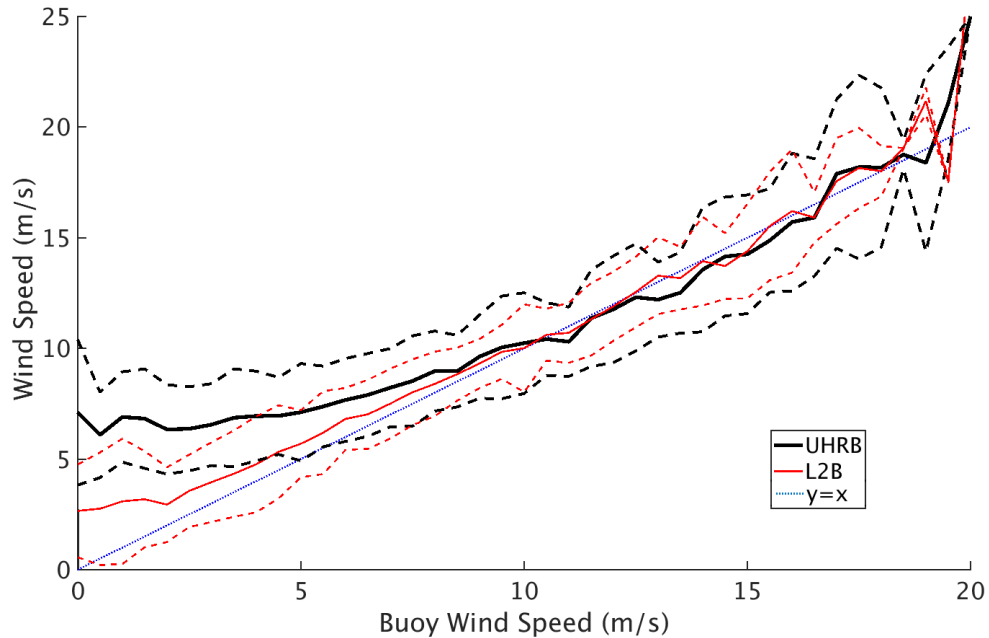
Figure 3.4: Plot of mean UHRB and L2B wind speeds (solid) with standard deviation (dashed) lines verses buoy wind speed. Mean UHRB wind speeds reveal a bias for low wind speeds. A $y = x$ line is included for reference.

UHRB direction estimates are not as tightly grouped around the $y = x$ line as the L2B direction estimates, confirming they are noisier. However, the UHRB winds tend to be within $\pm 90°$ more than L2B estimates for lower wind speeds. I emphasize that UHRB represents the best case scenario, in that it has "perfect" ambiguity selection. Nevertheless, the results demonstrate the potential of RapidScat UHR wind estimates in near-coastal regions. The L2B estimates used in the comparison use the ambiguity provided by NASA's Jet Propulsion Laboratory (JPL) and do not represent "perfect" ambiguity selections. In Section 3.5 the performance of the ambiguity selection direction is compared to buoy measurements.

3.2 Median Filter-Based Ambiguity Selection Scheme

As previously noted, the median filter-based ambiguity selection scheme is used to select a unique ambiguity at each WVC [23]. A median filter-based ambiguity selection scheme can smooth out the nudged wind fields while still preserving wind fronts [26]. The window size is an important consideration when designing the filter [24]. A variety of window sizes, ranging from
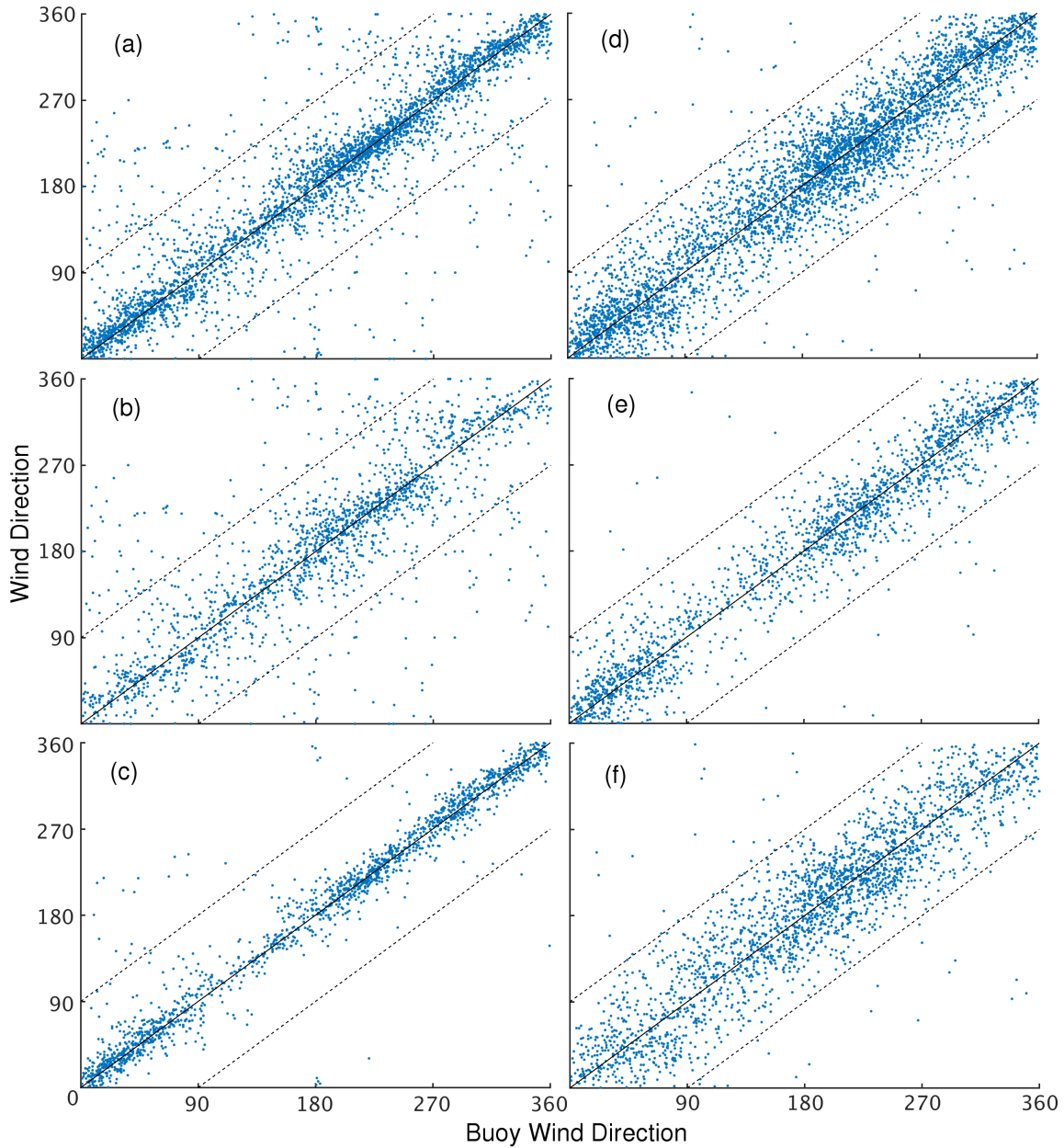
Figure 3.5: Plots of RapidScat L2B (a)–(c) and UHRB (d)–(f) wind directions with collocated buoy measurements sorted by wind speed. The top row presents collocations for all the wind speeds. The middle row shows the collocations with wind speeds below 7 m/s, while the bottom row shows collocations with wind speeds above 7 m/s. The dashed lines are $\pm$ 90° from the ideal $y = x$ line. Due to the circular nature of direction values, for clarity I shifted the points in the corners $x < 90$, $y > 270$ by -360 and $x > 270$, $y < 90$ by +360 in the y direction.

17
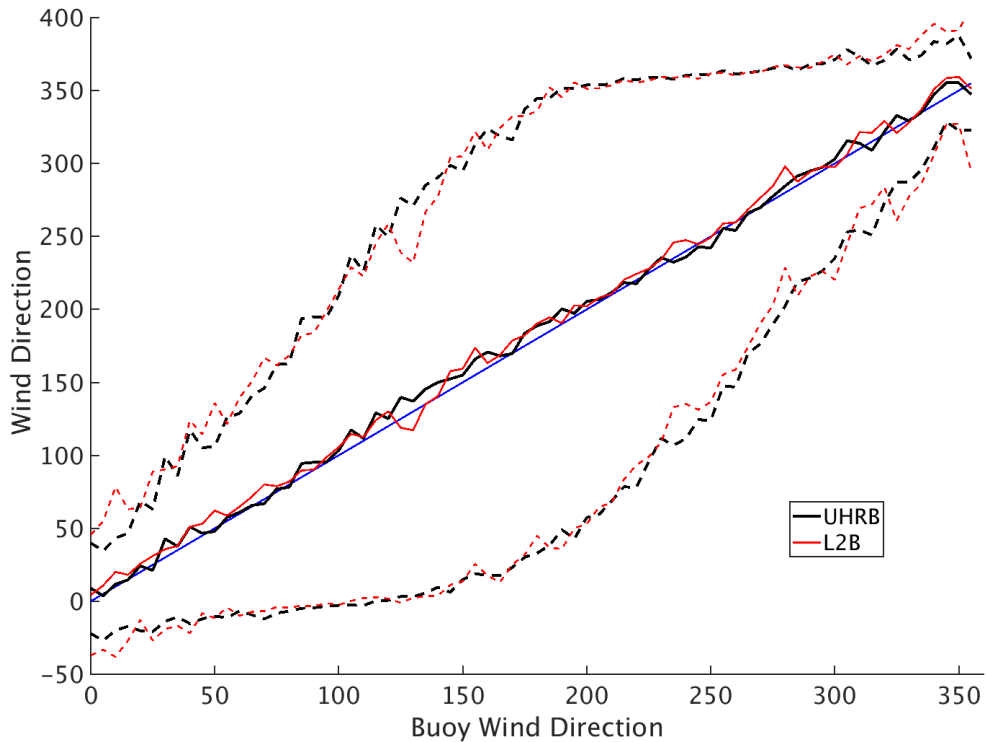
Figure 3.6: Comparison of UHRB and L2B circular mean directions (solid lines) with collocated mean buoy measurements. The dashed lines are one standard deviation of the angular difference from buoy measurements, see text.

17.5 km to 77.5 km, were tested for RapidScat UHR ambiguity selection. If the window is too small, inconsistencies can overwhelm the filter and result in large areas of inconsistent ambiguity choices. This generally occurs only in the nadir and far-swath. A window that is too small can also be blind to larger wind features. Excessively large filters are computationally taxing and have diminishing returns as far as improved accuracy is concerned. Another consideration is RMS difference from NWP winds. A comparison of the RMS difference from NWP wind directions for different median filter window sizes compared to L2B RMS differences is shown in Fig. 3.7. The figure shows that RMS difference decreases as filter size increases. Based on this analysis, a window size of 52.5 km is chosen (dashed line in Fig. 3.7). This corresponds to a 21 x 21 UHR WVC window. The 52.5 km window preserves both large and small wind features, lowers RMS difference, and has an acceptable computational burden.
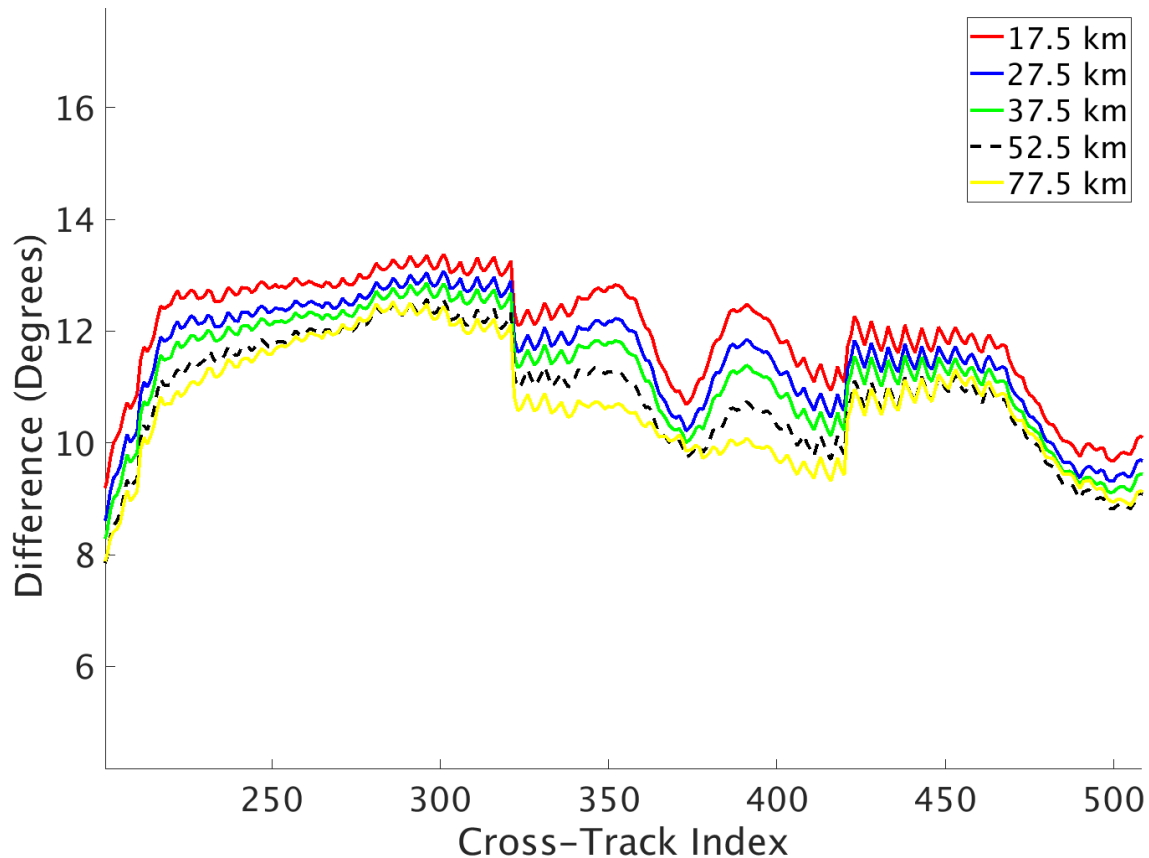
Figure 3.7: Difference between RMS difference (from NWP winds) of different median filter window sizes and RMS difference of L2B estimates.

3.3 DIR

DIR, while originally developed for conventional L2B data, can be applied to UHR wind retrieval to improve the wind estimates. A brief description of DIR is provided in this section. Another previously developed algorithm, thresholded nudging (TN), is briefly considered for Rapid-Scat application at the end of this section.

DIR was developed to improve wind estimation accuracy for QuikSCAT L2B estimates in the nadir region [21]. In this paper, the nadir region is defined to be within 125 km of the nadir track. As previously noted, the nadir region lacks the azimuth angle diversity required for accurate wind direction determination because the σ^0 measurement angles are close to 180° apart, see Fig. 2.2. The lack of azimuth diversity results in regions around the objective function's local maxima that are close to the value of the local maxima themselves, see Fig. 3.8. Typical of this problem, the objective function has a "wide" local maxima that incorporates a range of wind vec-

19

tors that yield similar objective function values. When this happens, the most spatially consistent wind estimate may not be associated with the objective function maximum, but may be nearby with a similar objective function value. This wide maxima effect is not specific to the nadir region, but is most commonly seen there.

Rather than reporting a single direction value for each ambiguity as in conventional wind retrieval, DIR captures the range of wind direction solutions that are similar in likelihood to the local maxima. The range of solutions are then used in a modified median filter-based ambiguity selection scheme that selects a spatially consistent value from within the range of solutions. Fortunately, there is little variation in wind speed around the area of the local maxima, so the wind speed assumed for the range of directions is the wind speed associated with its respective maximum.

Our implementation of DIR is performed by determining a range of directions around each local maximum. The range is defined by a boundary to either side of the local maximum. The endpoints of the boundary are found by taking a fraction of the value of the objective function at each local maximum to create a threshold, see Fig. 3.8. The fraction 0.2 was subjectively chosen; however the DIR algorithm is relatively insensitive to the precise fraction value. This value is adjusted to ensure a minimum of 30° between the endpoints. This use of minimum range differs from [21].

To compute the DIR range, the routine iterates along the objective function at 1.0° steps on either side of the local maximum until the threshold is reached. When the objective function reaches the threshold on either side, the respective directions are used as the endpoints for the range of directions around each local maxima. The more confident local maxima, i.e., ones that have a steeper gradient around the local maxima themselves, have a smaller distance between the endpoints. Broad local maxima have a wide range of direction solutions with similar likelihood, with endpoints that are further apart, see Fig. 3.8. The wind directions associated with each local maximum are saved along with the DIR ranges. The directions associated with the local maxima are used for the nudged field that initializes the ambiguity selection. Our implementation of DIR differs from [21] who used a fixed threshold, whereas I use a threshold that is varied under certain circumstances.

The DIR-modified ambiguity selection follows the baseline ambiguity selection procedure until an ambiguity is chosen. Once an ambiguity is selected, a new closest-to-median value is
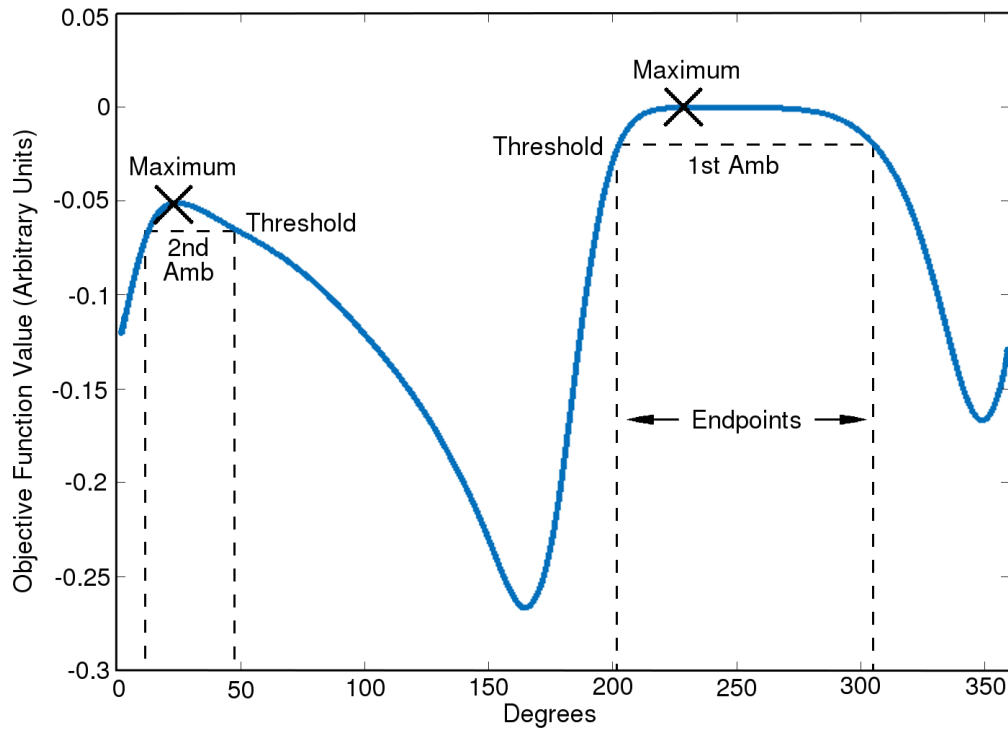
Figure 3.8: Example objective function with two local maxima, arbitrarily placed thresholds, and the resulting endpoint boundaries (the vertical dashed lines).

chosen from the DIR range of directions associated with the chosen ambiguity. The DIR range is spaced at 1.0° steps. A variety of steps were tested and the 1.0° interval proved to be computationally efficient, while providing similar results compared to the finer resolution steps.

The direction within the DIR range closest to the circular median of the local median filter window is chosen to replace the direction for the chosen ambiguity of the center WVC, see Fig. 3.8. If the difference between the chosen value from between the endpoints is greater than 5° from the current ambiguity direction, the ambiguity choice is updated and the direction for that ambiguity is changed to the value chosen from between the endpoints; otherwise the value is not changed. This process, like the baseline median filter-based ambiguity selection scheme, continues until it converges or the maximum number of iterations (200) is reached. Occasionally, the algorithm does not converge, but oscillates between sets of values. When the number of changed ambiguities in an iteration remains the same for five iterations in a row the process is terminated. The number of

21

changed ambiguities when this happens is typically less than 50 out of a swath with thousands of WVCs.

Even when using DIR, nadir WVCs can still have inconsistent ambiguity choices. To ameliorate the inconsistencies, the threshold for nadir WVCs is adjusted to increase the distance of each endpoint from the maxima by 15° on either side. Adjusting the threshold provides additional flexibility in creating consistent fields. Fig. 3.9 shows how the modified DIR improves the wind estimates in the nadir region, resulting in a more consistent, smoother field.

I note that the DIR threshold can fall below all possible values of the objective function. In the case that endpoints are not found because the threshold does not intersect the objective function, an arbitrary DIR range of $\pm 15°$ from the ambiguity's direction is assigned.

While TN was also developed for, and used in, QuikSCAT processing, I do not use TN in the RapidScat UHR nudging process. TN is designed to improve the accuracy of ambiguity selection in the far-swath, which it does by changing the number of ambiguity selection choices when generating the nudged field. Because there are typically fewer ambiguities available in the far-swath for RapidScat, TN's limiting the number of ambiguities has little effect on those regions for RapidScat.

3.4 Dealing With WVCs With Only a Single Ambiguity

The limited azimuth diversity, upwind/downwind asymmetry in the nadir region, and noise can result in some WVCs having only a single ambiguity. Approximately 1.6% of all WVCs in a RapidScat swath have only a single ambiguity after the wind retrieval process and greater than 99% of all WVCs with only a single ambiguity are found within 125 km of the nadir track.

Unfortunately, WVCs with only one ambiguity create complications when trying to generate a consistent wind field. WVCs with only one ambiguity have no flexibility to blend in with surrounding WVCs and tend to force the ambiguity selection, but they are often noisy. Even with DIR applied, inconsistencies due to single ambiguity WVCs persist, see Fig. 3.9 (the dark spots are WVCs with a single ambiguity).

The direction associated with single ambiguity WVCs is often inconsistent with the optimum wind field, though most are consistent with the first ambiguity choices (the ambiguity with the highest likelihood value out of the four) of WVCs surrounding them. This is evident in Fig. 3.10,
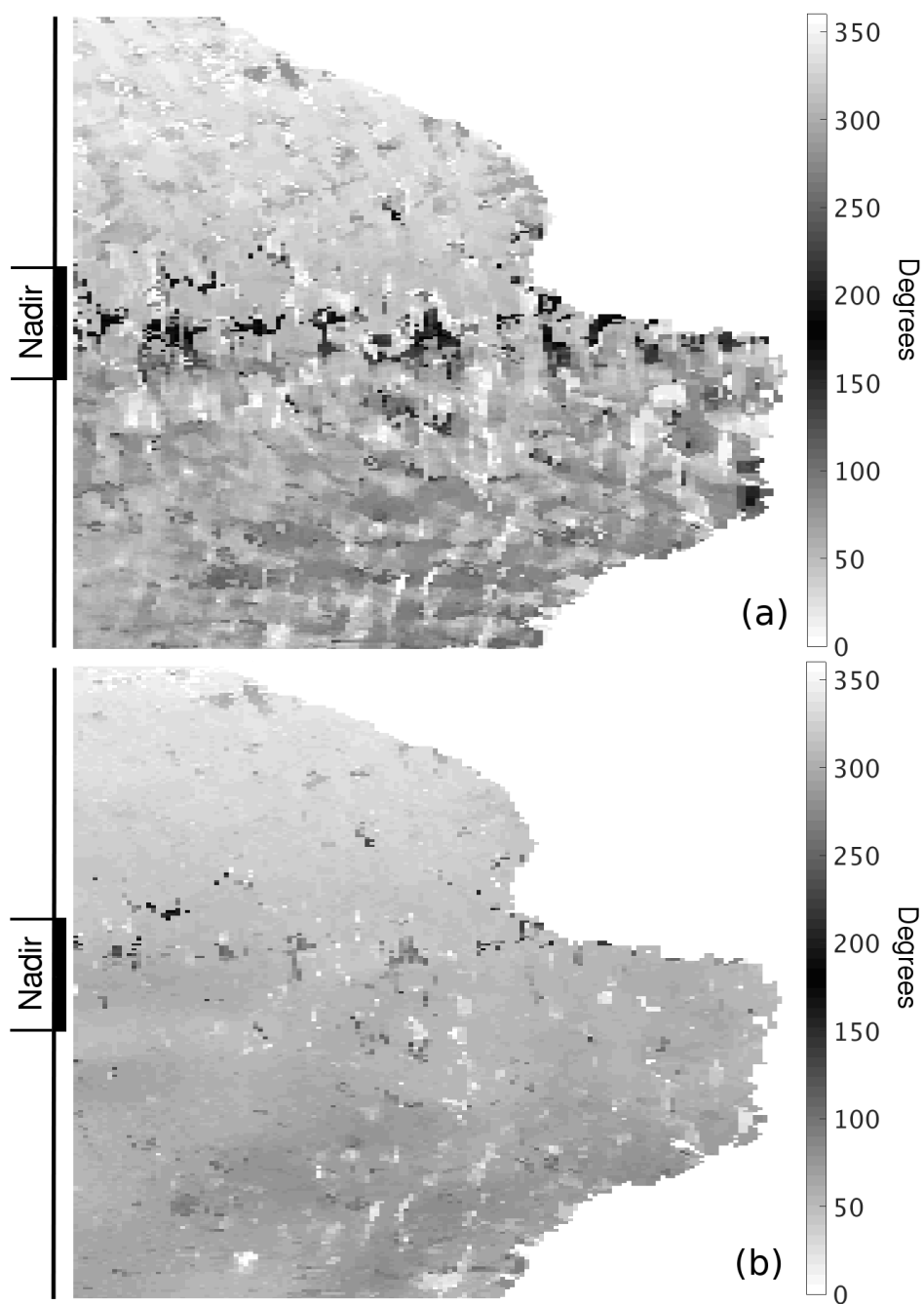
Figure 3.9: Images of selected UHR wind directions before and after DIR is applied. The 425 x 625 km direction field shown includes part of the nadir region of the swath. The white area is land. (a) shows the nudged UHR field without a median filter-based ambiguity selection scheme applied. (b) shows the same region with the DIR modified ambiguity selection scheme applied. The colorbar shows the direction of each location in degrees. Many WVCs with inconsistent directions in the nudged UHR field have the flexibility to become more consistent after DIR is applied.

which shows a direction field composed of only the first ambiguity choices for each WVC. The nadir track is visible where the angles that are about 180° apart meet.
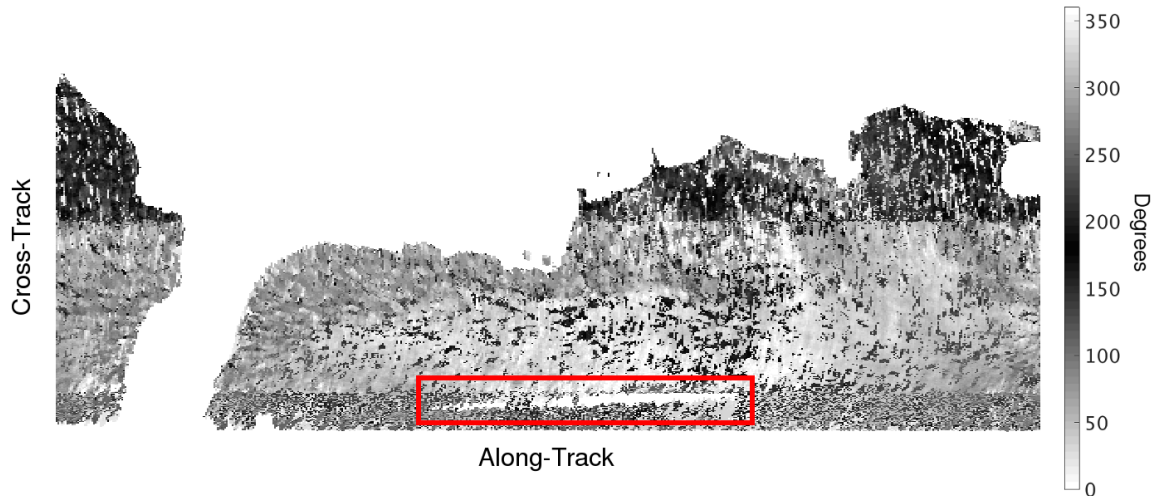
Figure 3.10: Direction field of a portion of a swath showing only the first ambiguity choices for all WVCs. The directions on either side of the nadir track are approximately 180° apart. WVCs with only a single ambiguity lie in the areas just on either side of the center dividing lines and are not distinguishable from the ambiguities around them. The long white patch in the boxed region is a data gap resulting from sector blanking.

Fig. 3.11 shows a histogram of the average difference between the direction of single ambiguity WVCs with the directions of the first ambiguities surrounding it within a 3 x 3 WVC window. A total of 958,582 WVCs with a single ambiguity are taken from 18 different swaths to create this plot. A majority of the WVCs with a single ambiguity have an average difference less than 50° from the surrounding WVCs. This confirms that the directions associated with single ambiguity WVCs are generally consistent with other first ambiguities.

To improve the accuracy of WVCs with a single ambiguity I arbitrarily add two "artificial" ambiguities (AA) to WVCs with only one ambiguity. Analysis of multiple revs shows that the average number of ambiguities in WVCs surrounding single ambiguity WVCs is two or three. Two ambiguity WVCs were most common in the nadir region, so I experimented first with adding a single artificial ambiguity (for a total of two) that has the same wind speed and is 180° away from the original ambiguity, with a DIR range of ± 15°. However, spatial inconsistencies still persist in the nadir region with the addition of only one ambiguity. I found that adding two AA (for a total
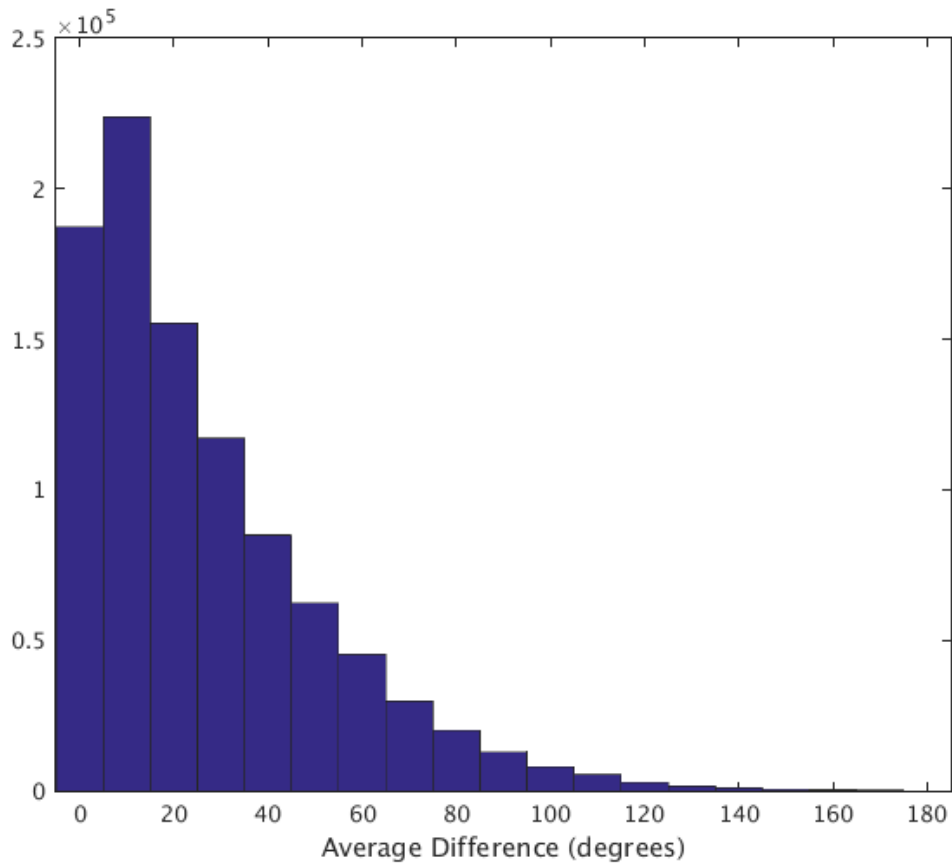
Figure 3.11: Histogram of the average difference in direction between WVCs with a single ambiguity and the surrounding first ambiguity choices in a 3 x 3 WVC window.

of three) produced better results. The two AA are set to $\pm$ 120° from the original ambiguity with a DIR range of $\pm$ 15° and are assigned the same wind speed as the single ambiguity. Fig. 3.12 (a) shows WVCs with a single ambiguity from one nudged field swath collocated with NWP winds. Fig. 3.12 (b) shows the same WVCs after AA are added to the DIR wind retrieval process, note the improved correlation. The result is a much stronger correlation, which is visible by how much closer it follows the $y = x$ line. I conclude that adding AA to single ambiguity WVCs improves the selected wind direction accuracy. UHR estimates with AA are further validated in the next section.
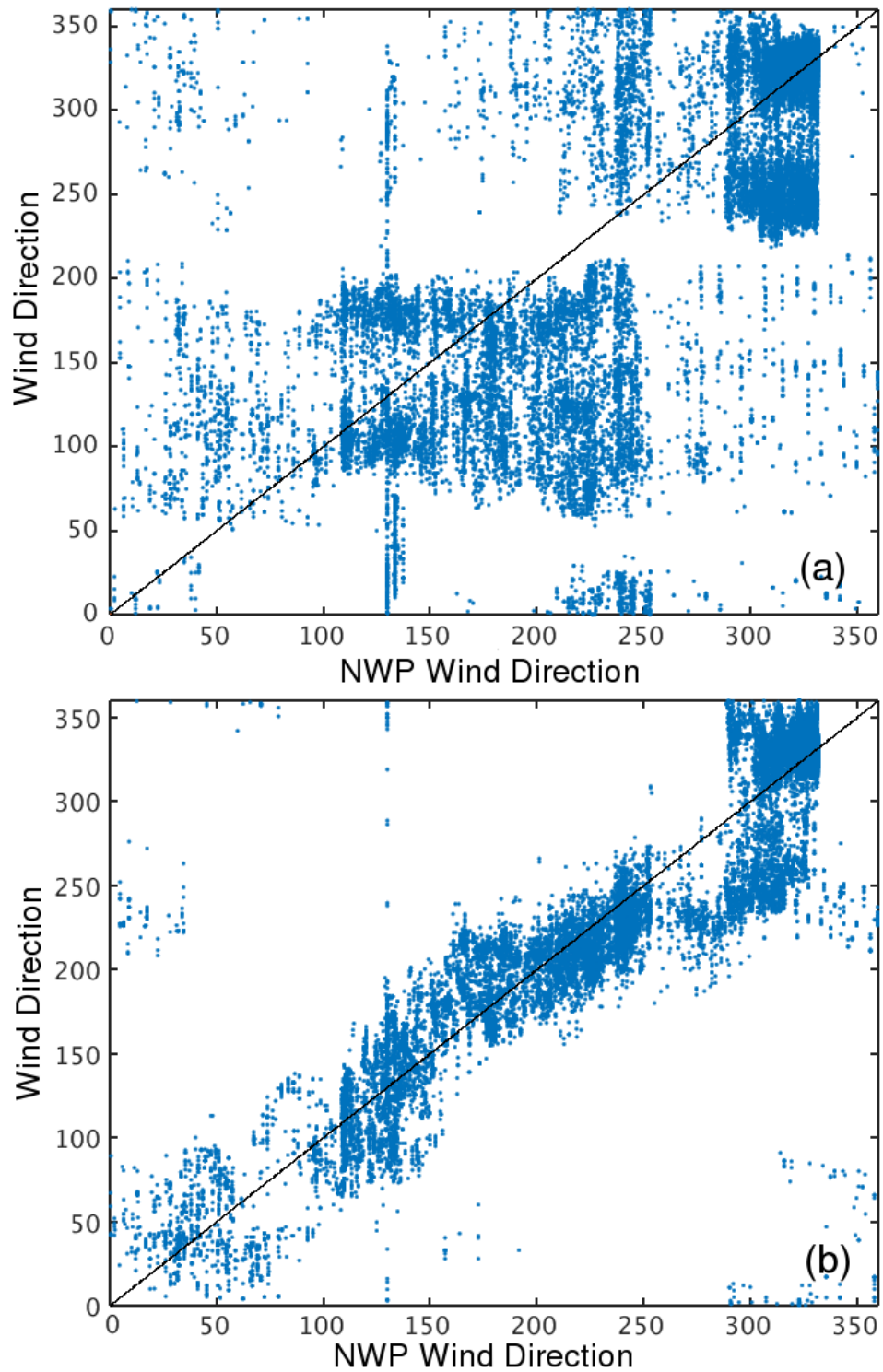
Figure 3.12: Scatter plots of wind direction for (a) WVCs with a single ambiguity from one swath plotted against collocated NWP winds and (b) the same collocations, but processed with DIR and AA. Note the improved correlation with the NWP winds in (b).

3.5 Validation of Near-Coastal UHR estimates with DIR and AA

RapidScat UHR wind estimates with DIR and AA (hereafter referred to as UHRAA) are validated using the same approach as the UHRB near-coastal validation described in Section 3.1. An analysis of the wind speed accuracy is described in Section 3.5.1. The results of the wind direction comparison are in Section 3.5.2.

3.5.1 UHRAA Wind Speed Accuracy

In this section, I consider UHRAA wind speed validation. Fig. 3.13 shows UHRAA and L2B wind speeds plotted against collocated NDBC buoy measurements. As was done in Section 3.1, the UHRAA estimates are averaged over a 5 x 5 window to better match the resolution of the lower resolution measurements. The UHRAA estimates are slightly more concentrated around the $y = x$ for estimates between 5 and 10 m/s than the UHRB estimates in Section 3.1. Despite the higher concentration around the $y = x$ line, Fig. 3.14 shows that, on average, the UHRAA wind speed estimates are slightly higher than the UHRB estimates (compare to Fig. 3.3). The UHRAA estimates cross the 10% threshold multiple times in the wind speed range from $8 - 20$ m/s. Fig. 3.15 shows UHRAA, UHRB, and L2B mean wind speeds. UHRAA means closely follow UHRB mean values. The similarity between the UHRAA and the UHRB results suggest that the modified UHR ambiguity selection algorithm is choosing the close-to-optimal ambiguities.

3.5.2 UHRAA Wind Direction Accuracy

An analysis of UHRAA wind direction is detailed in this section. Fig. 3.16 shows UHRAA wind direction estimates collocated with offshore buoy measurements. L2B collocated measurements are plotted again for convenience. The dashed lines in the plot represent a 90° difference from buoy measurements. UHRAA estimates are noisier than the ideal UHRB estimates in Fig. 3.5, but still match up fairly well with the L2B estimates. Noticeable improvement can be seen for estimates above 7 m/s. At higher wind speeds the UHRAA estimates are grouped tighter around the $y = x$ line than UHRB direction estimates. For wind speeds below 7 m/s the UHRAA estimates appear more spread out than UHRB estimates.
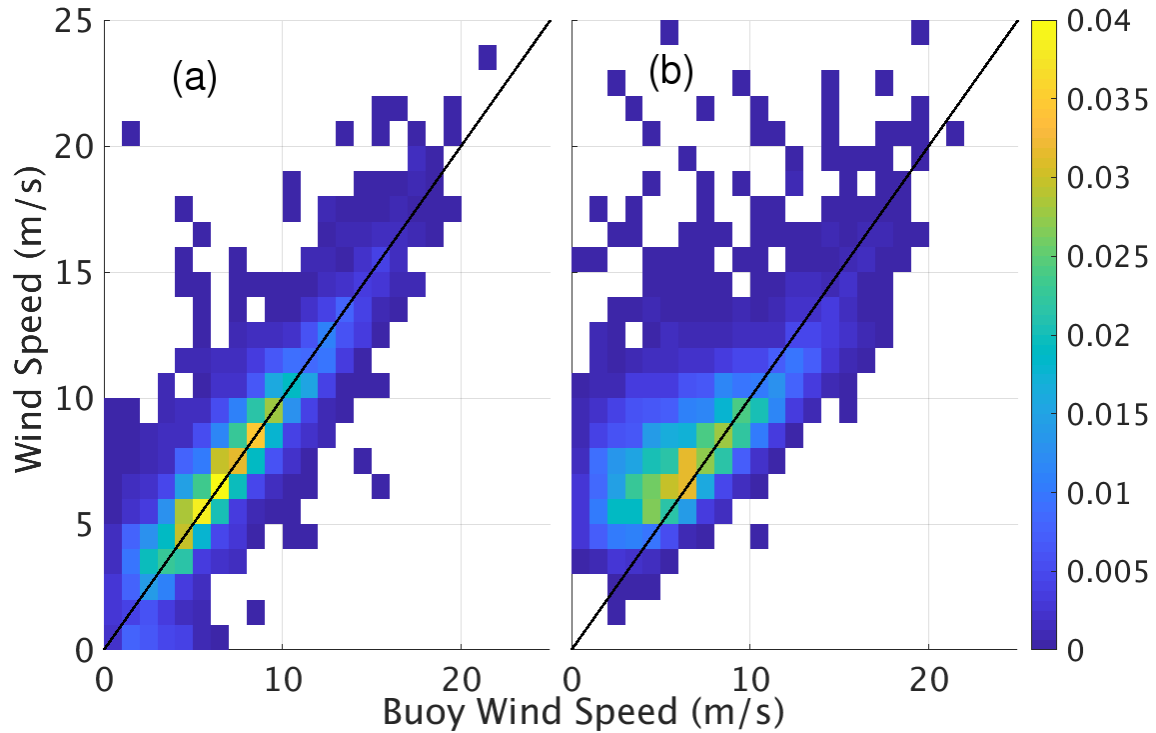
Figure 3.13: Scatter density plots of L2B (a) and UHRAA (b) wind speeds plotted against collocated buoy wind speed measurements. The UHRAA estimates have a tighter fit around the $y = x$ line for winds in the range of $5 - 10$ m/s compared to the UHRB estimates, compare Fig. 3.2.

Fig. 3.17 shows the mean directions of UHRAA and L2B estimates binned at $5°$. Both the UHRAA and L2B mean lines closely follow the $y = x$ line. Like UHRB estimates, the UHRAA standard deviation line of the difference closely follows the L2B standard deviation line. Fig. 3.18 shows the root-mean-square (RMS) difference between different versions of UHR wind direction estimates and L2B wind direction estimates compared to NWP winds. The plot includes RMS values for a month's worth of L2B, UHR nudged, UHR with DIR, but without AA (UHRD), and UHRAA estimates. UHRD decreases the RMS difference across the swath, especially in the nadir region. UHRAA further decreases in RMS in the nadir region even more. The RMS across the swath for all wind speeds is decreased by the algorithm improvements. A visual inspection also confirms these results. Fig. 3.19 shows a section of L2B, UHR nudged, and UHRAA processed winds along the East Coast of the United States. The UHR nudged field is noisier than the L2B and some of the wind features are difficult to distinguish. UHRAA reduces the noise in the nudged field, while preserving the L2B wind features at a higher resolution.

28
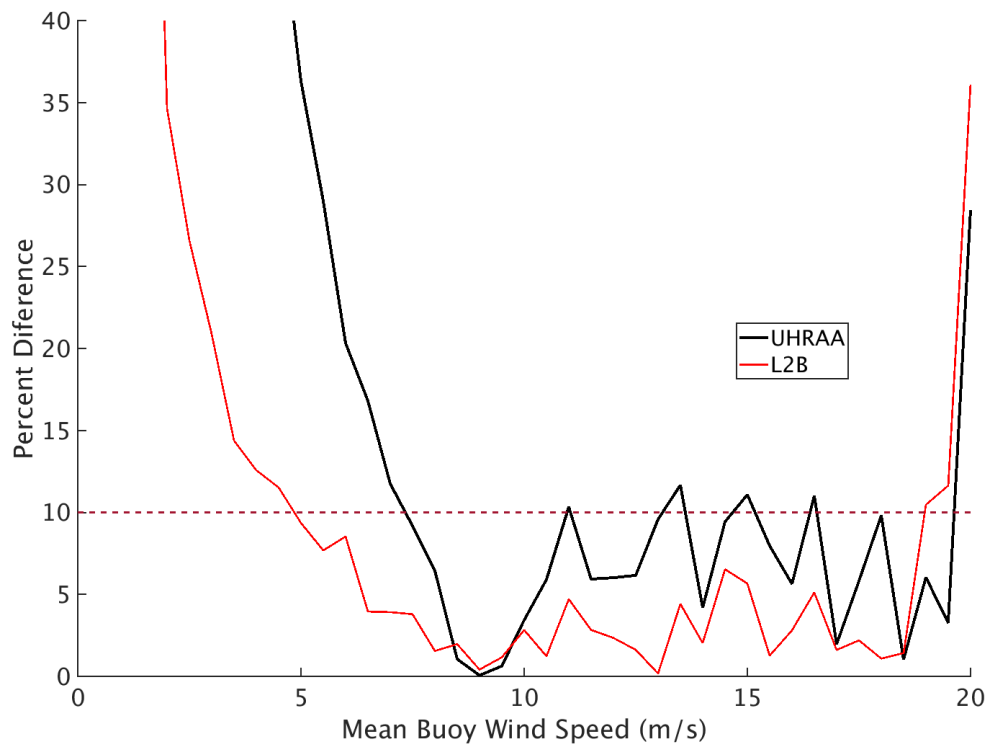
Figure 3.14: Percentage difference of mean L2B and mean UHRAA estimates from mean buoy measurements. The horizontal dashed line shows the 10 percent difference boundary. For wind speeds greater than 7 m/s, the UHRAA estimates have about twice the error of L2B wind speed estimates.
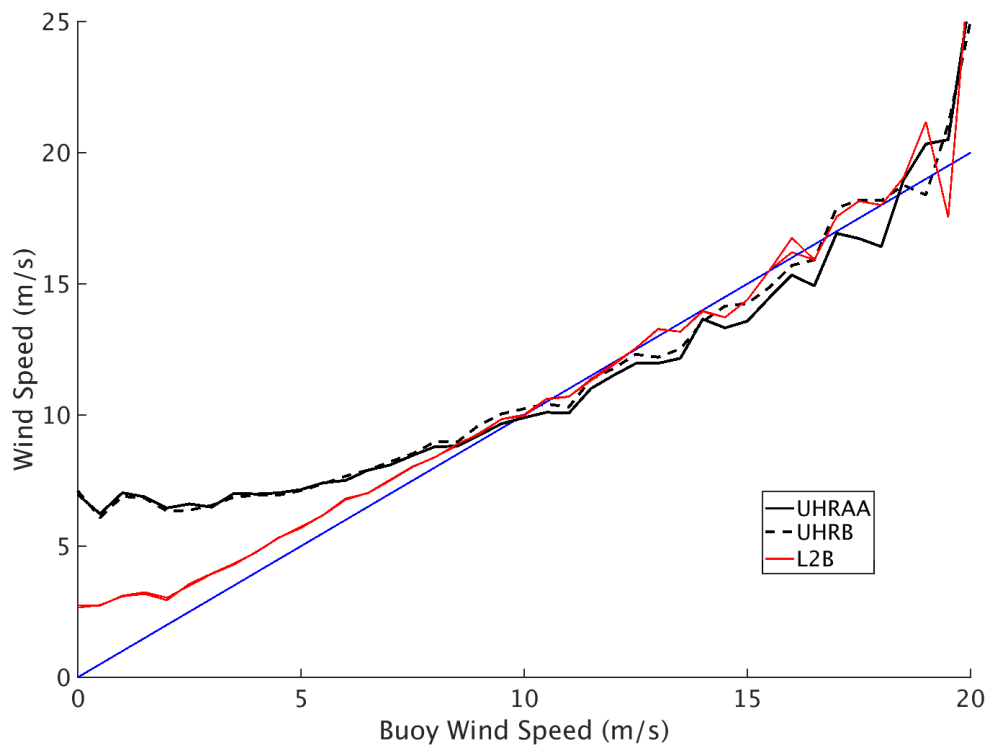
Figure 3.15: Mean UHRAA, UHRB, and L2B wind speeds verses collocated mean buoy wind speeds.
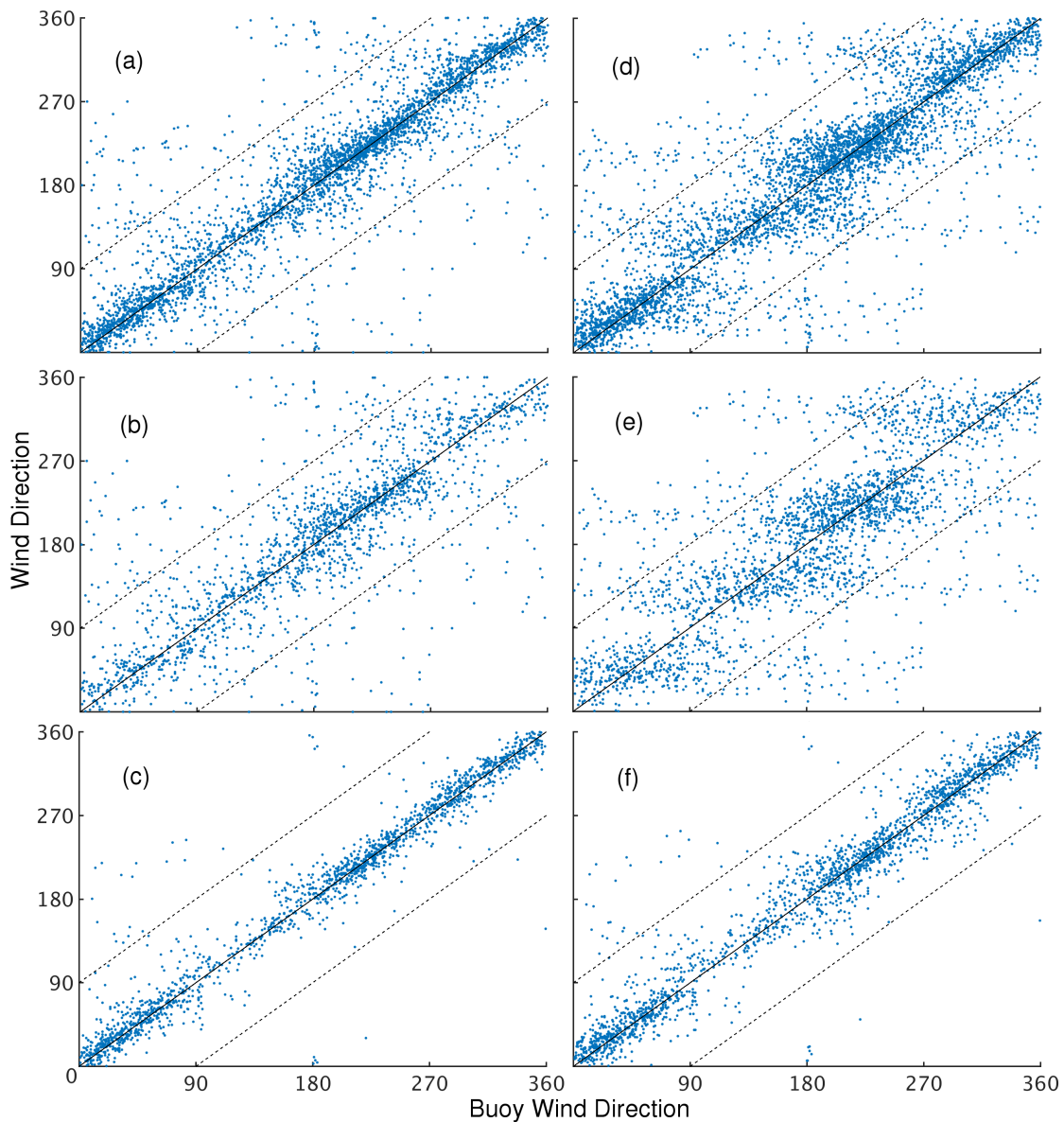
Figure 3.16: Scatter plots of RapidScat L2B (a)–(c) and UHRAA (d)–(f) wind directions with collocated buoy measurements sorted by wind speed. The top plots present collocations at all wind speeds. The middle row shows the collocations with wind speeds below 7 m/s and the bottom row shows collocations with wind speeds above 7 m/s. The dashed lines in each plot show a difference of 90° from the ideal $y = x$ line. Due to the circular nature of direction values, for clarity I shifted the points in the corners $x < 90$, $y > 270$ by -360 and $x > 270$, $y < 90$ by +360 in the y direction.
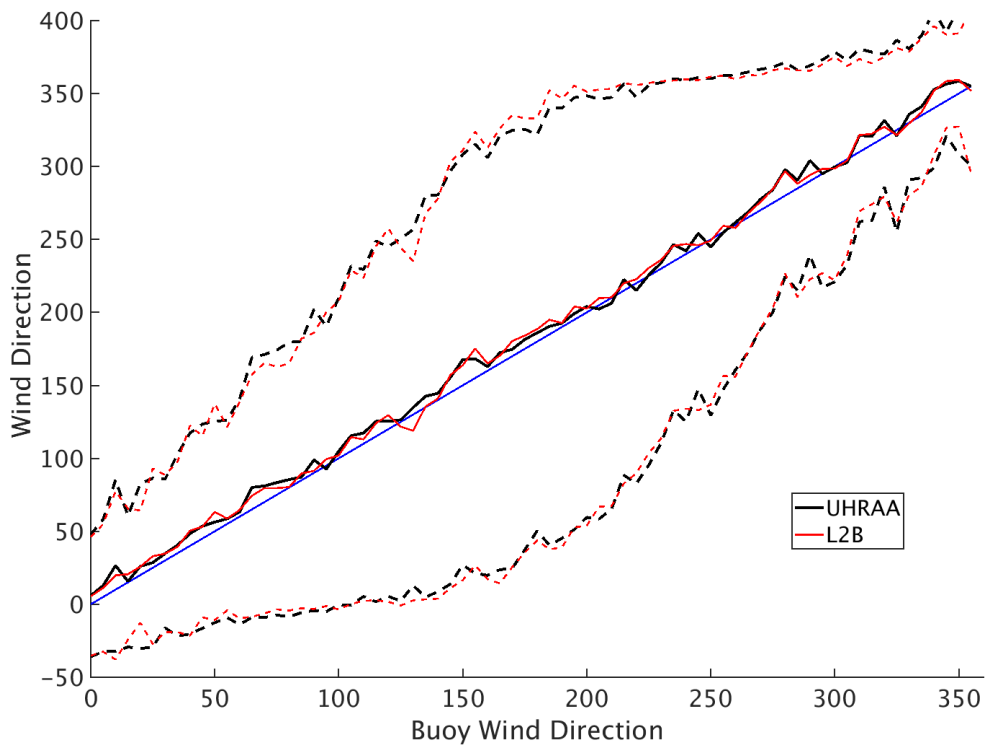
Figure 3.17: Plot of the circular means for UHRAA and L2B wind directions collocated with buoy measurements. Included also is a $y = x$ line and a one standard deviation line of the angular difference for both UHRAA and L2B (dashed lines).
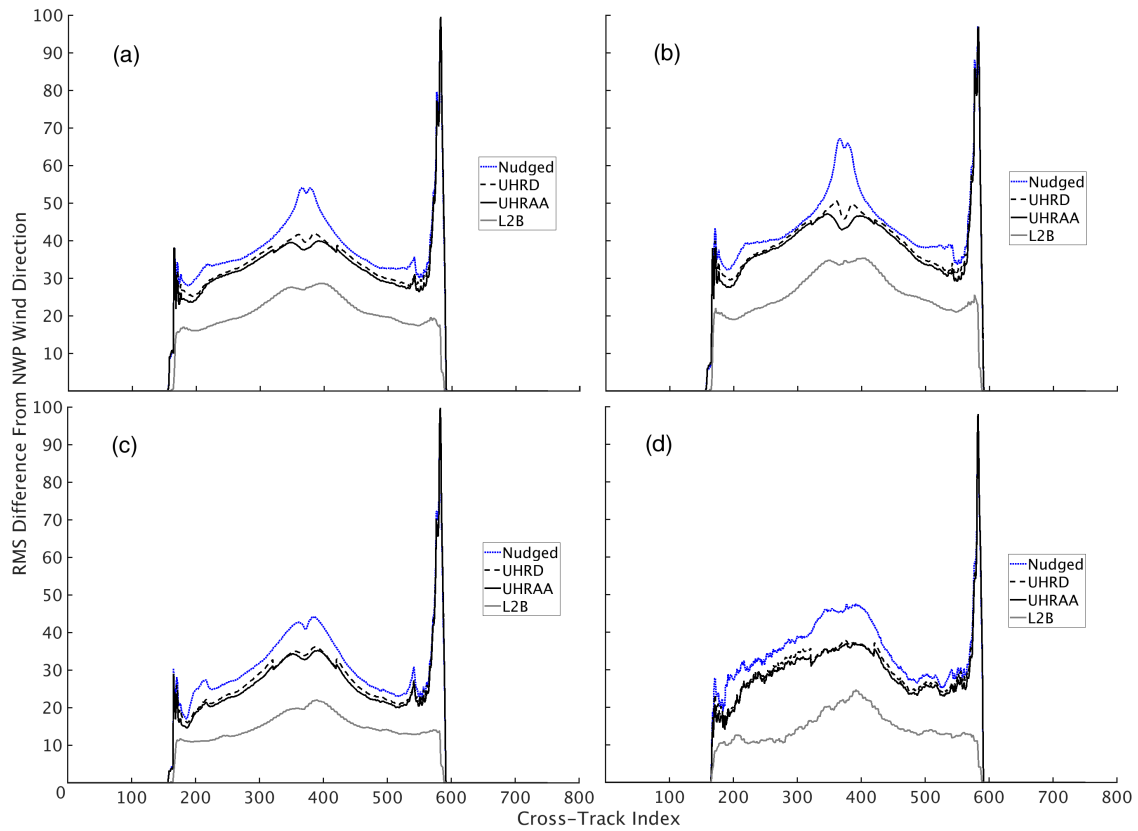
Figure 3.18: RMS difference between different versions of UHR wind estimates and NWP sorted by wind speed and plotted against cross-track WVC number. RMS difference between L2B and NWP is also included in each plot. (a) includes all wind speeds, (b) wind speeds below 8 m/s, (c) wind speeds 8 − 15 m/s, and (d) has collocations with wind speeds greater than 15 m/s. Adding the median filter-based ambiguity selection scheme lowers the RMS value across the swath for all wind speeds. The addition of AA lowers the RMS in the nadir for all wind speeds.
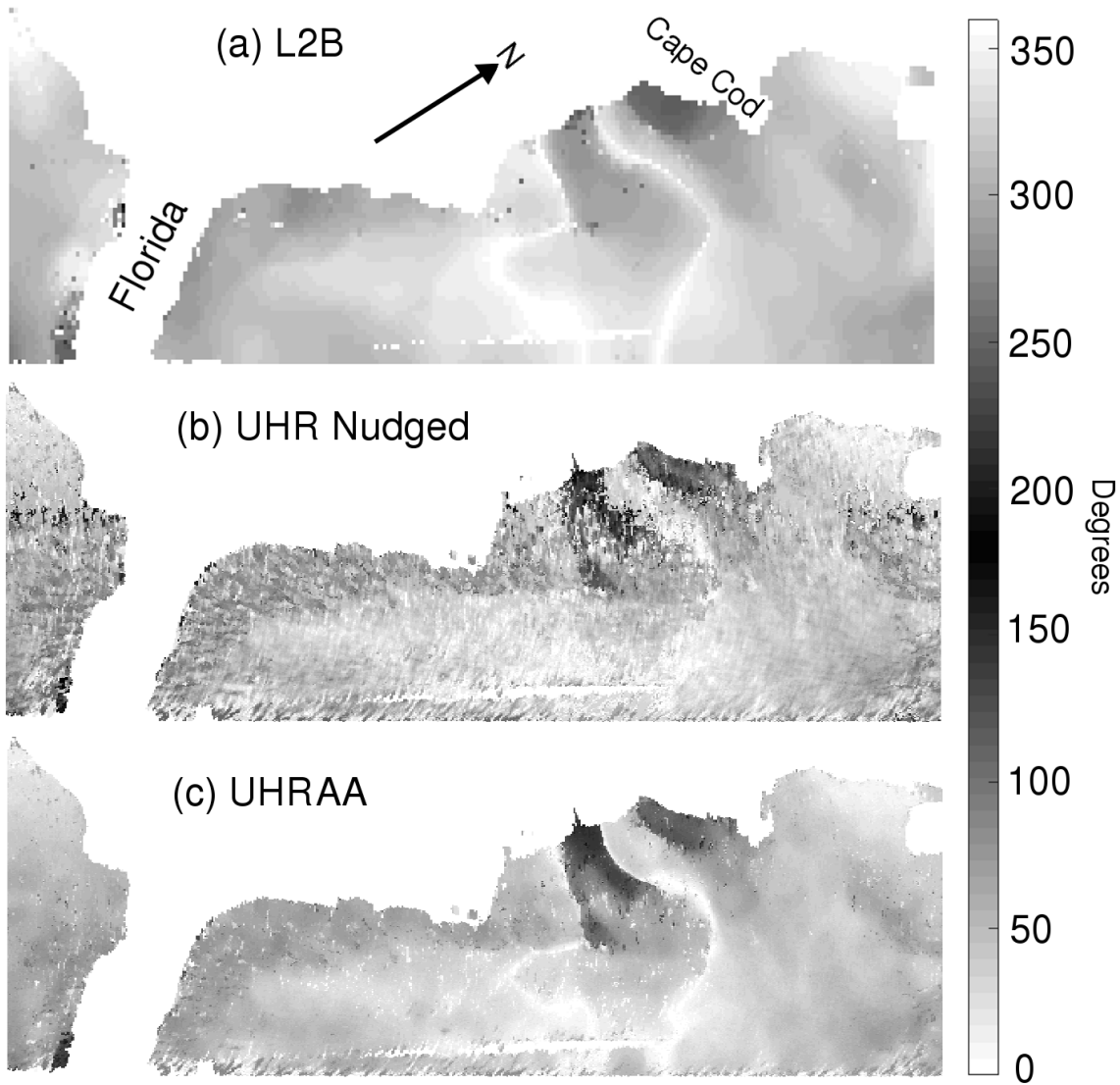
Figure 3.19: L2B (a), UHR nudged (b), and UHRAA (c) wind direction fields. The swaths are 1877.5 km by 2777.5 km on the East Coast of the United States, see text.

CHAPTER 4.   WIND ESTIMATION NEAR THE HAWAIIAN ISLANDS

4.1   Wind Estimation Near the Hawaiian Islands

Wind directions in the lee of the Big Island can run counter to the prevailing trade winds, exhibiting a reverse flow. The reverse flow has been both observed [27–29] and modeled [12, 30]. The reverse flow can be seen in numerical wind models created by the Asia Data Pacific Research Center (ADPRC) [31].

The ADPRC wind model is referred to as the Hawaii regional climate model (HRCM), a model which predicts vector winds hourly on a 3 km grid near the Hawaiian islands [30–32]. HRCM winds are adapted from the Advanced Research Weather Research and Forecasting model to fit the Hawaii region. HRCM winds use 25 km QuikSCAT wind speed estimates, among other data sets, as an input [30].

Fig. 4.1 is an HRCM wind field from a summer day and shows all the wind features expected in this area. Fig. 4.1 shows trade winds blowing around the two peaks of the Big Island creating pockets of high wind speed to the north and south of the island and a low wind speed tail in the lee (west side) of the island. The low wind speed tail is where the reverse flow is found. In this case, the model shows a reverse flow resulting from the formation of one vortex. Often multiple vortexes (counter clockwise and/or clockwise) contribute to the reverse flow. The locations of the vortexes vary with changing wind flow.

Generally, as in Fig. 4.1, the reverse flow is found on the west side of the island. However, the reverse flow phenomenon can be observed on other sides of the island, depending on changing wind flows. The angle and length of the reverse flow region depends on the direction and speed of the prevailing wind flow. The reverse flow can extend as far out as 50–100 km from the shore [27, 33].

The reverse flow region is difficult to resolve for traditional 12.5 km grid resolution QuikSCAT and ASCAT L2B wind processing because of the complex fine resolution wind direction features
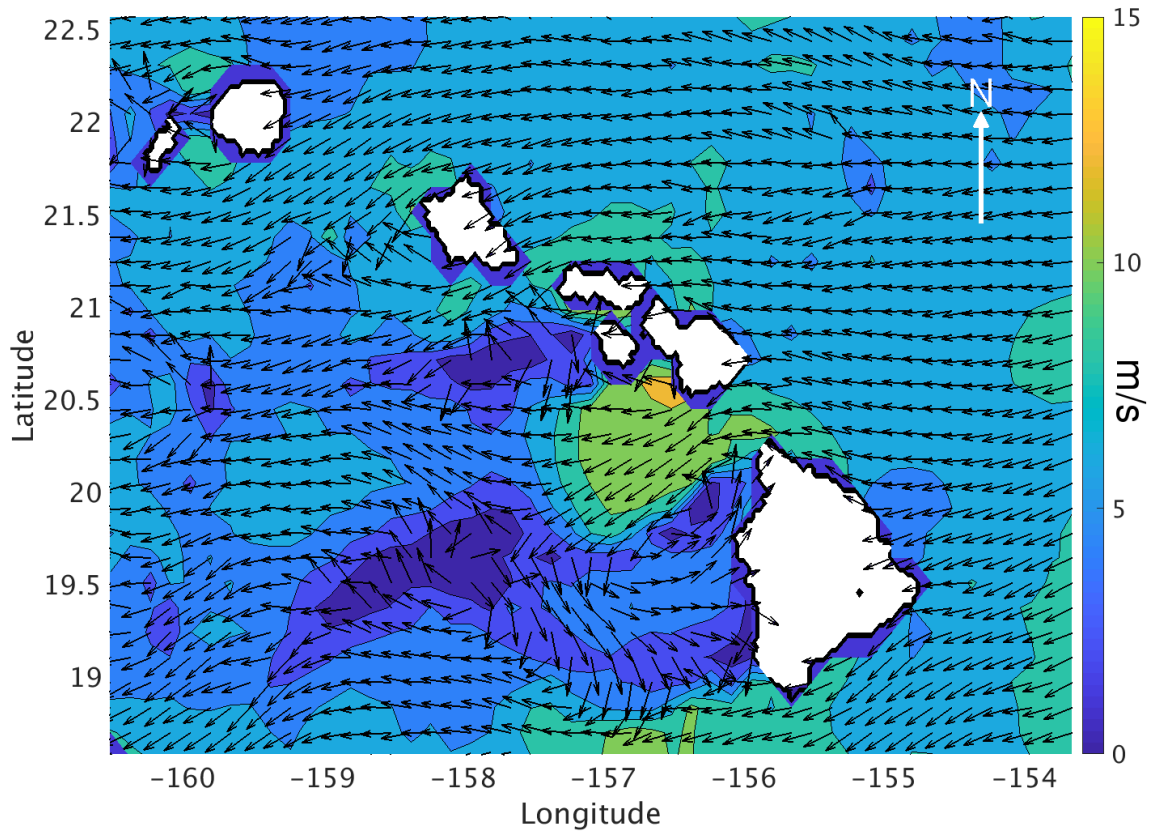
Figure 4.1: An example HRCM 3 km hourly wind vector field. Wind direction quivers are downsampled and unit length. The contour shows the wind speed in m/s. The land mask is shown in white. The reverse flow can be seen on the west side of the Big Island. The wind field is from 03:00 June 26, 2003.

and the low wind speed [25, 33]. UHR capabilities of both sensors are shown with simple examples. L2B comparisons are shown alongside for reference. A more in depth look at scatterometer and model winds follows.

To illustrate QuikSCAT L2B and UHR (reported on a 2.5 km grid) capabilities, Fig. 4.2 shows QuikSCAT L2B (a) and UHR (b) wind fields that are collocated within 30 minutes of the model field in Fig. 4.1. Compared to the model winds the low wind speed tail and high wind speed pockets are partially resolved. The reverse flow seen in the HRCM predicted winds (Fig. 4.1) is not seen in either QuikSCAT wind field. Fig. 4.2 shows that QuikSCAT UHR winds with DIR better resolve some features compared to L2B, but are still unable to fully resolve all the features when compared to HRCM winds. As described later, a land contamination buffer, especially in the L2B wind field, prevents wind retrieval close to the island.
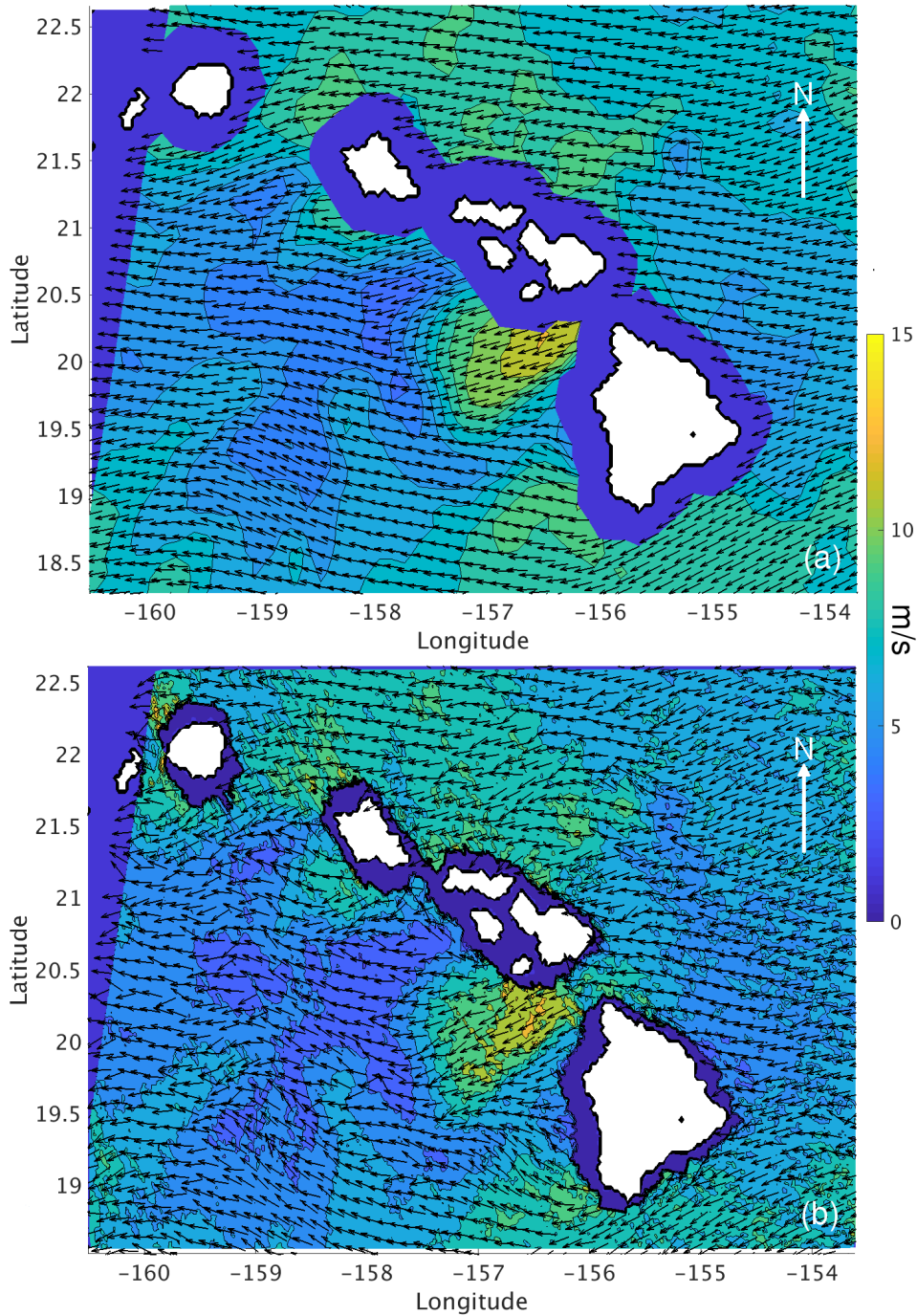
Figure 4.2: An NWP nudged QuikSCAT L2B wind vector field (a) and an L2B nudged QuikSCAT UHR wind vector field with DIR (b). Wind direction quivers in each panel are unit length. UHR wind direction quivers are downsampled for clarity. The contours show the wind speed in m/s. A land mask is shown in white in both panels. In (a) L2B wind estimates within 30 km of land are discarded due to the proximity to land. In (b) a land contamination correction is used to retrieve UHR winds closer to shore than the L2B (Section 4.2 explains the land buffer in more detail). This QuikSCAT pass is from June 26, 2003 (orbit 20918).

Similarly, in Fig. 4.3 ASCAT L2B and UHR (1.25 km grid) wind fields are compared with an HRCM wind field. The ASCAT wind fields are measured within 10 minutes of the HRCM predicted wind shown in the Fig. 4.3 (a). The L2B wind field shown in Fig. 4.3 (b) and the UHR field in (c) both partially resolve the low wind speed tail and high wind speed pockets compared to the model. ASCAT UHR (1.25 km grid) better resolves some features compared to L2B but still is insufficient according to HRCM winds. The reverse flow and vortexes predicted in the HRCM wind field in (a) are not resolved in either wind field.

In Section 4.2 a more in depth comparison between the scatterometer winds (L2B and UHR, QuikSCAT and ASCAT) and HRCM winds is outlined. The goal of the comparison is to better understand current UHR capabilities in the near-coastal region of Hawaii. In Section 4.3, scatterometer measured σ^0 are compared to predicted model σ^0 to further compare the data sets. Section 4.4 shows the effects of the nudging field and median filter-based ambiguity selection scheme on UHR scatterometer wind fields. Conclusions are discussed in Section 4.5.

4.2   Winds in the Lee of the Big Island

QuikSCAT and ASCAT passes from January 1, 2007 to December 31, 2008 are considered for comparison with HRCM winds. The high variability of winds in the reverse flow region necessitates a close temporal collocation. In the analysis, QuikSCAT passes must be within 10 minutes and ASCAT passes within 20 minutes of the HRCM wind fields to be used. ASCAT orbits have a different collocation time because of a low number of orbits that are within 10 minutes. Additionally, passes must sufficiently cover the region of interest. Fig 4.4 shows the region of interest (between 20.50° and 18.75° latitude and -154° and -158° longitude) around the Big Island. For consistency, only scatterometer orbits with usual trade wind flow (around 270°) that puts the reverse flow on the west side of the island are considered. From those years (2007 and 2008), a total of 276 QuikSCAT and 236 ASCAT passes are studied.

It is important to note that HRCM winds exhibit wind speeds well below 5 m/s, a range where scatterometers are less accurate since low wind speeds are difficult to process due to lower SNR [25]. Scatterometer winds below 2 m/s are considered unreliable.

HRCM estimates winds near and over the islands; however, scatterometer wind retrieval is limited to the ocean sufficiently far from land. For this reason, comparisons with L2B or UHR
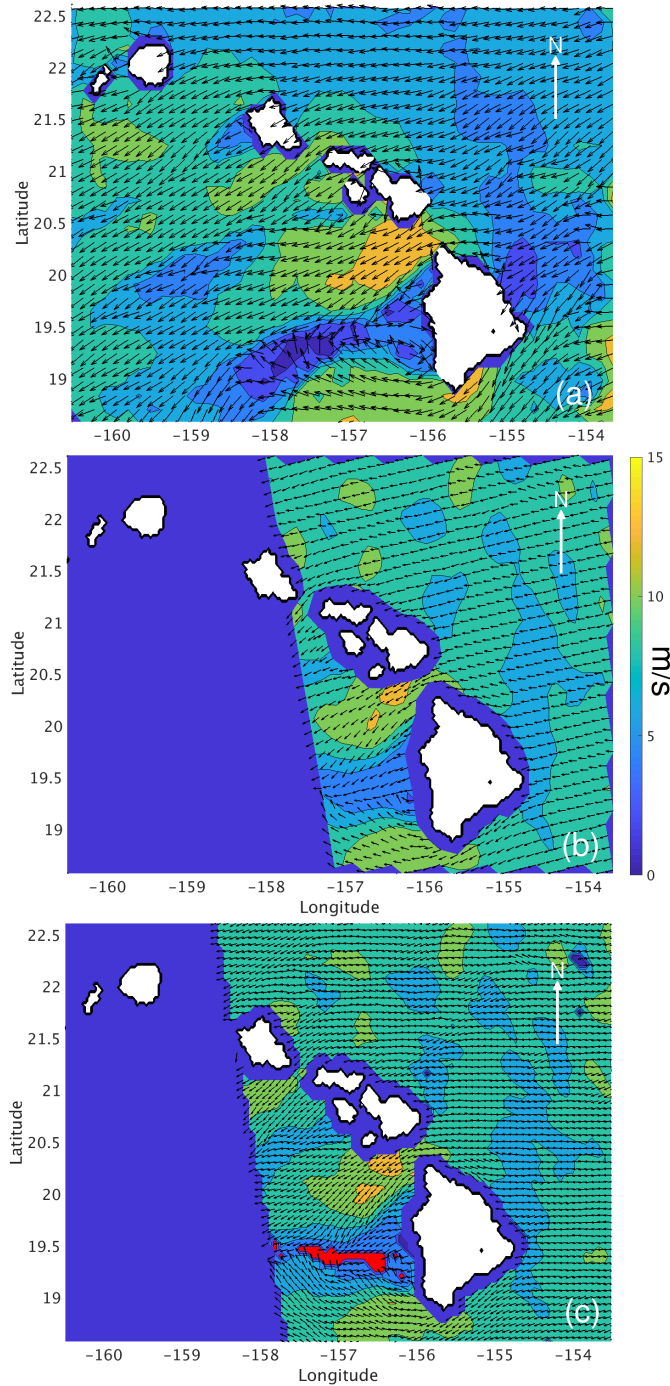
Figure 4.3: HRCM wind field (a) collocated with ASCAT L2B (b) and UHR (c) wind fields. Wind direction quivers in each panel are unit length. HRCM and UHR wind direction quivers are downsampled for clarity. Land masks are shown in white in all panels. Appropriate land buffers are shown in each panel as well. The red region in (c) is where wind estimates were discarded due to poor wind retrieval. Many ASCAT UHR swaths have some estimates lost due to poor retrieval conditions in the lee area. (a) is from HRCM 08:00 July 2, 2007. The ASCAT pass is from July 2, 2007 (orbit 3631) and is collocated within 10 minutes of (a).

winds consider only HRCM winds outside of the land buffers. For L2B, the land buffer is a fixed 30 km zone. UHR employs land contamination correction and yields accurate estimates closer to the land than L2B [9].
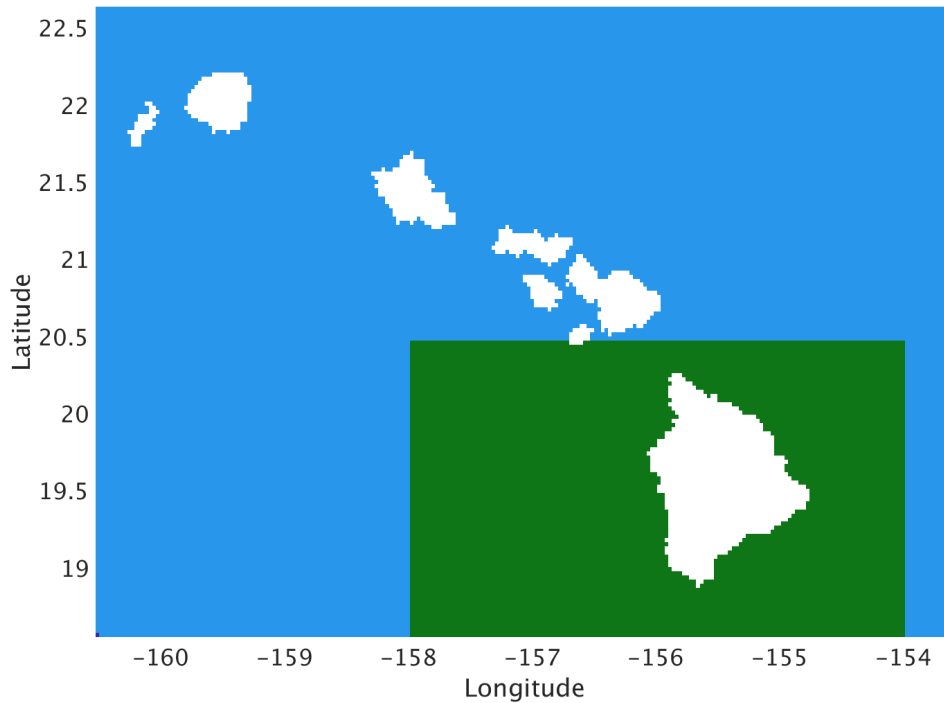
Figure 4.4: The region of interest for the study is shown in yellow. Land is shown in white and ocean in blue.

4.2.1 Comparison of Wind Speed and Direction

First, QuikSCAT L2B wind speeds and directions are compared with HRCM winds. Next, QuikSCAT UHR wind speeds and directions are compared with the HRCM winds. The section concludes with a comparison of ASCAT L2B and UHR wind vectors with HRCM winds.

Fig. 4.5 (a) is a density plot of QuikSCAT L2B wind speeds in the study area versus HRCM wind speeds. HRCM winds are collocated within 12.5 km of the QuikSCAT L2B winds. QuikSCAT L2B wind speeds appear to overestimate wind speeds in the region compared to the model, especially at low wind speeds. Fig. 4.5 (b) compares L2B and HRCM wind directions. The directions of the L2B estimates are consistent only with the trade wind flow (about 270°) even

when the model shows a reverse flow. The HRCM wind directions also span all directions 0°–360°. This is partially due to vortexes in the HRCM winds. In contrast, L2B wind directions span a relatively narrow band of wind directions showing that the mean flow dominates the L2B wind field.

Fig. 4.6 (a) shows the collocated QuikSCAT UHR wind speeds versus the HRCM wind speeds (all collocations are within 2.5 km). The UHR wind speeds are similar to the L2B distribution. Fig. 4.6 (b) compares the QuikSCAT UHR wind directions with HRCM wind directions. From the figure it is apparent that, like the L2B winds, the trade winds (around 270°) dominate the UHR wind direction field. The UHR wind field does not have the variety of directions that HRCM includes and UHR winds do not show the reverse flow.

Fig. 4.7 (a) shows collocated ASCAT L2B wind speeds plotted versus HRCM wind speeds. HRCM winds are collocated within 12.5 km of the ASCAT L2B winds. The distribution of wind speeds is similar to that of QuikSCAT but matches better at higher and lower wind speeds. ASCAT wind directions are plotted versus collocated with HRCM wind directions in Fig. 4.7 (b). The trade wind trend seen in the QuikSCAT wind directions is seen in the ASCAT L2B wind directions as well. Fig. 4.8 shows ASCAT UHR wind speeds (a) and directions (b) plotted versus HRCM winds (all collocations are within 1.25 km). ASCAT UHR winds show similar trends for both wind speed and direction as have been seen in previous figures.

4.2.2 Summary

These figures show that scatterometer winds (especially wind directions) do not match well what the HRCM winds predict. In particular, scatterometer winds do not show the reverse flow and vortexes. While the HRCM winds do show reverse flow and vortexes, the actual locations of any vortexes and reverse flow cannot be verified. With no truth data it is difficult to draw too many conclusions from the above analysis. These results do show, however, that the reverse flow and vortexes are not resolved in current UHR wind retrieval. In the following section, I turn to an analysis of σ^0 to further compare UHR products with the HRCM.
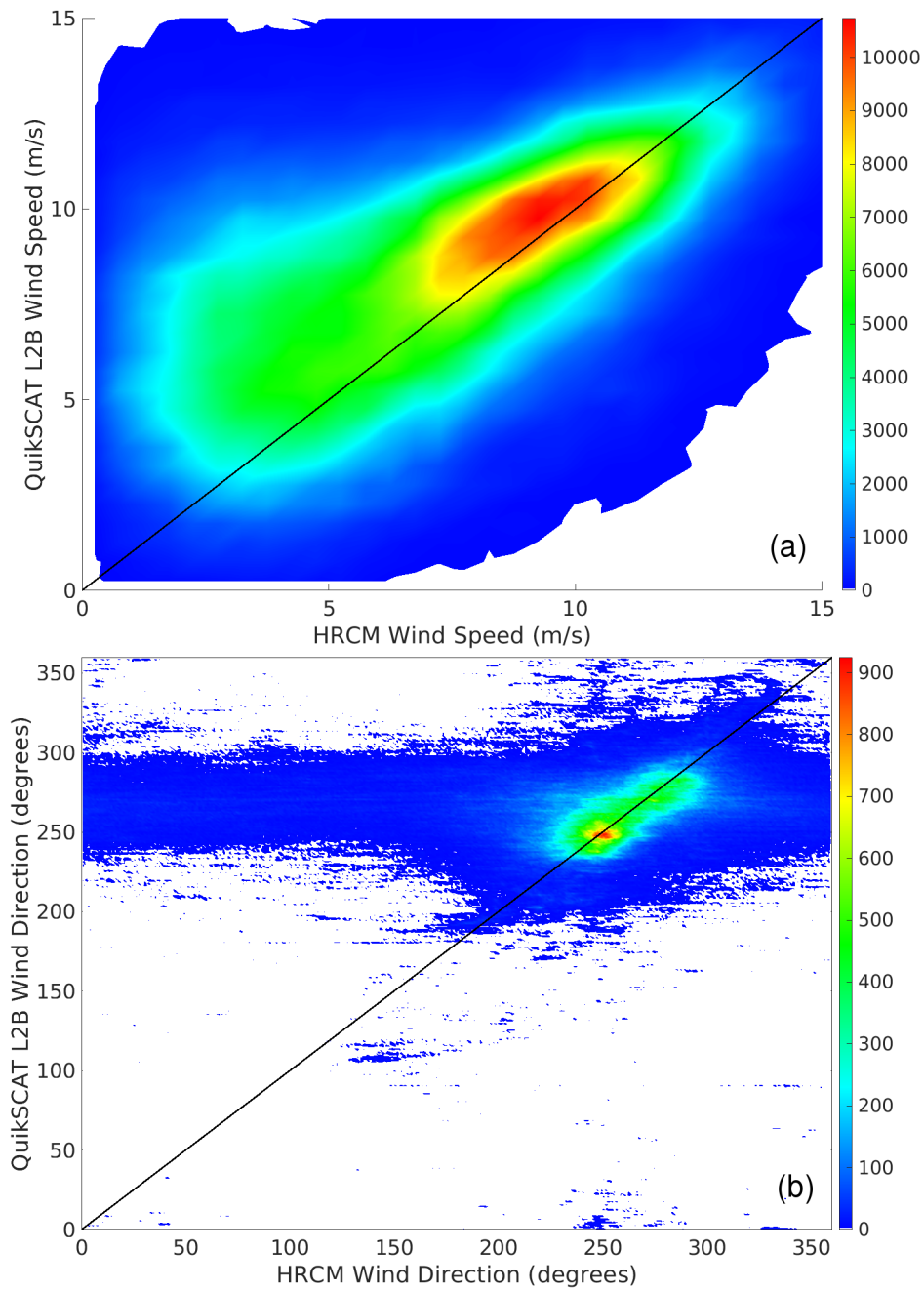
Figure 4.5: Density plots of QuikSCAT L2B and HRCM winds. (a) is a plot of L2B wind speeds versus the HRCM wind speeds. (b) shows L2B wind directions versus HRCM wind directions. A $y = x$ line is included in each plot for reference.
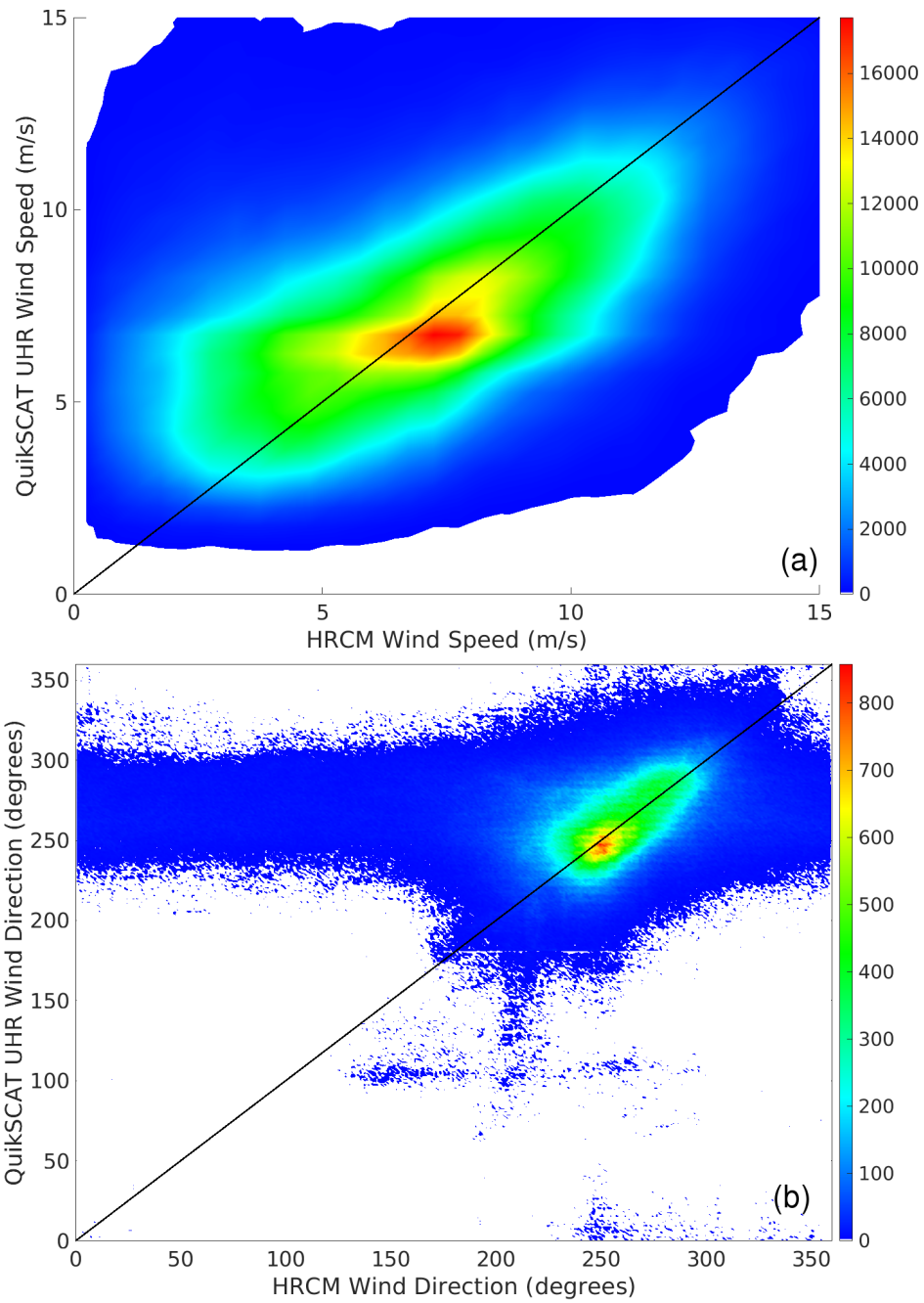
Figure 4.6: Density plots of QuikSCAT UHR wind speeds (a) and directions (b) plotted versus HRCM winds. A $y = x$ line is included in each plot for reference.
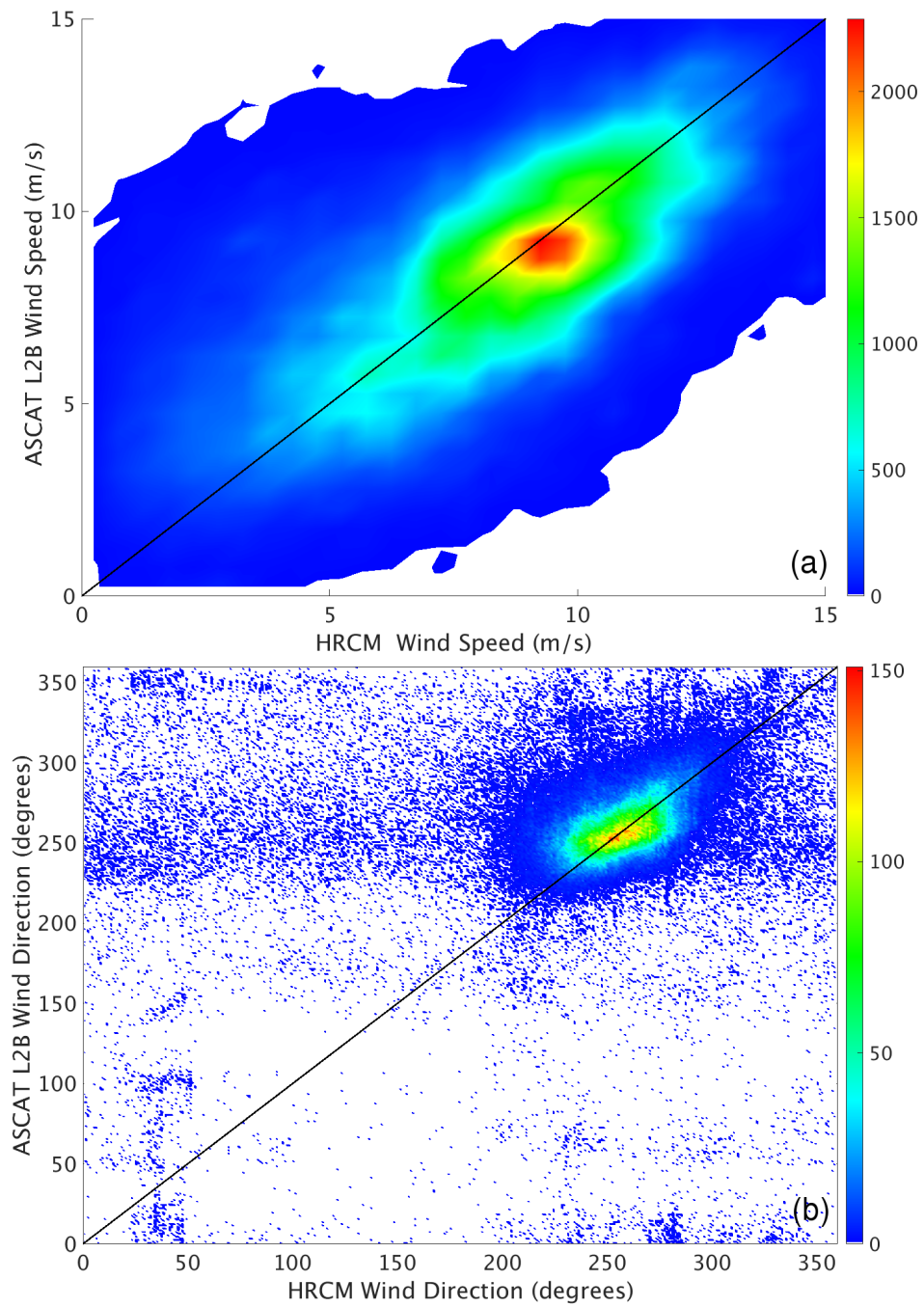
Figure 4.7: Comparison of ASCAT L2B and HRCM winds. (a) is a plot of L2B wind speeds versus the HRCM wind speeds. (b) shows L2B wind directions versus HRCM wind directions. A $y = x$ line is included in each plot for reference.
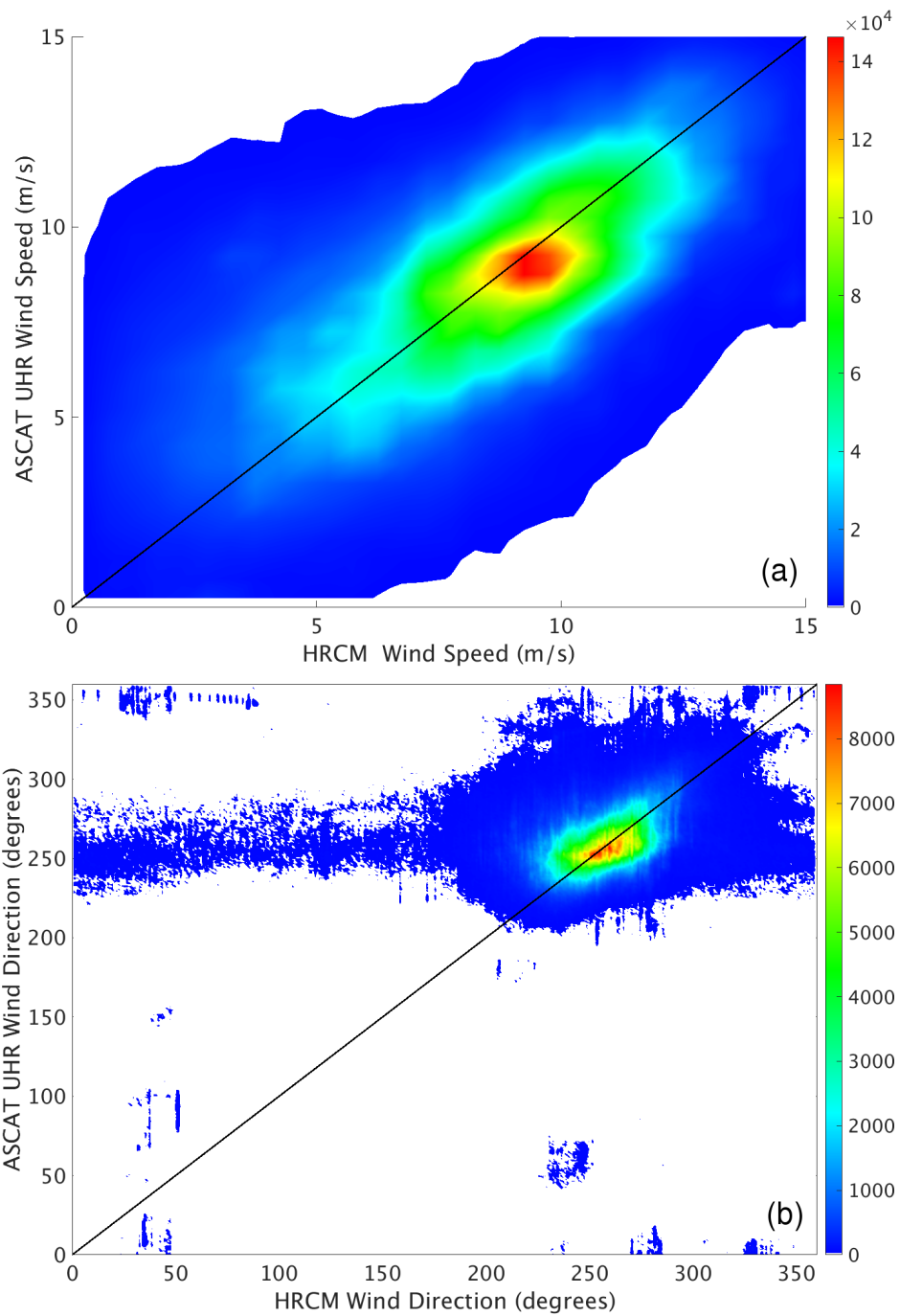
Figure 4.8: ASCAT UHR wind speeds (a) and directions (b) collocated with HRCM winds. A $y = x$ line is included in each plot for reference.

4.3 Comparison of Scatterometer Measured σ^0 and Predicted σ^0

Scatterometer measured σ^0 are useful to compare because they are actual measurements. The measurements are noisy, but they are unaffected by imperfect wind retrieval and ambiguity selection routines.

Two sets of HRCM and NWP predicted σ^0 are generated using the QuikSCAT QMOD3 [14] and ASCAT CMOD5 [34]. The area of interest for this study is the same as in Fig. 4.4. For consistency, only scatterometer passes with traditional trade wind flow (around 270°) that puts the reverse flow on the west side of the island are considered. The same temporal collocation criteria are used in this comparison as in Section 4.2.1. However, additional stipulations are added to both scatterometer passes that are considered for this study.

QuikSCAT's rotating pencil beam results in changing antenna look angles across the swath. Thus, only QuikSCAT passes with similar antenna look angles are considered. Similarly, ASCAT's left and right swaths have sufficiently different azimuth angles and need to be compared separately. Further, the incidence angle of fan beam scatterometers changes across the swath for each beam so passes over Hawaii should be compared with like incidence angles. Only the left swath measurements and passes with similar azimuth angles over Hawaii are used in this study. A total of 104 (similar look angles) QuikSCAT orbits and 44 (left swath and similar incidence angles) ASCAT orbits are examined below. First, QuikSCAT is compared HRCM and NWP predicted σ^0 in Section 4.3.1; a comparison between ASCAT σ^0 and predicted σ^0 from the models follows in Section 4.3.2.

4.3.1 QuikSCAT Versus Predicted σ^0

The average difference between the QuikSCAT measured σ^0 and HRCM QMOD3 predicted σ^0 for each "flavor" of σ^0 is shown in Fig. 4.9 (a)–(d). The four flavors of σ^0 for pencil beam scatterometers are vertical polarized fore looking (VF), vertical polarized aft looking (VA), horizontal polarized fore looking (HF), and horizontal polarized aft looking (HA). The flavors are analyzed separately because of the different effects azimuth angle and polarization have on σ^0. The first row in Fig. 4.9 shows VF, second VA, third HF, and the fourth row shows HA. Despite the differences in the high wind speed pocket regions, both polarizations immediately behind the

island generally agree, as seen by the similar low mean differences west of the Big Island. This is expected because even if the two data sets have different orientations for the low wind speed tail, the part immediately behind the island is common between them. However, the low difference is interesting because the QuikSCAT final selected winds in this area are generally 180° opposite HRCM in that area. The σ^0 agreeing in this area suggests that QuikSCAT σ^0 can be detecting the reverse flow, even if the selected QuikSCAT wind directions do not match the model winds there.

Fig. 4.9 (e)–(h) shows the standard deviation of the difference between the σ^0 normalized by QuikSCAT average wind speeds. I normalize with respect to QuikSCAT average wind speeds because σ^0 values are more variable as wind speed increases. This normalization for example lowers standard deviation values in high wind speed areas and keeps values in low wind speed areas relatively the same. Thus, partially removing the effect of wind speed on the comparison. The plots of the average wind speed for QuikSCAT and ASCAT and a brief discussion on them are found in Section 4.3.3. In (e)–(h) the standard deviation is the highest in the southern high wind speed pocket area. The variation in the differences suggests west of the island suggest that HRCM's predicted wind tail and reverse flow features do not match what QuikSCAT is detecting. The low standard deviation directly west of the island indicates that both wind fields are consistently close in that area. The low difference and low standard deviation values in this area show that QuikSCAT is possibly detecting a reverse flow. The differences to the east of the Big Island are likely from a wind front that the models show resulting from the trade winds hitting the side of the island.

The differences between the two data sets are clearly dependant on azimuth angle as seen by the "mirroring" of the differences in the north and south high wind speed pocket areas (see Fig. 4.9). The effect of azimuth angle on σ^0 is explained below with some ASCAT measurements near the Big Island. I show this with ASCAT measurements and NWP predicted σ^0 because of how clearly they illustrate the effect.

As explained in Chapter 2, σ^0 is a function of wind speed and χ. As wind speed increases so does the variability of σ^0 with respect to χ. This can be seen in Fig. 4.10 (a) in the plotted CMOD5 σ^0 curves. At 5 m/s σ^0 varies little as χ changes. In contrast, at 15 m/s σ^0 can span a much larger range of values as χ changes.

In Fig. 4.10 panels (a)–(c), σ^0 at the north high wind speed pocket (in red) and σ^0 taken at the south high wind speed pocket (in blue) location are plotted versus χ. The wind speeds and
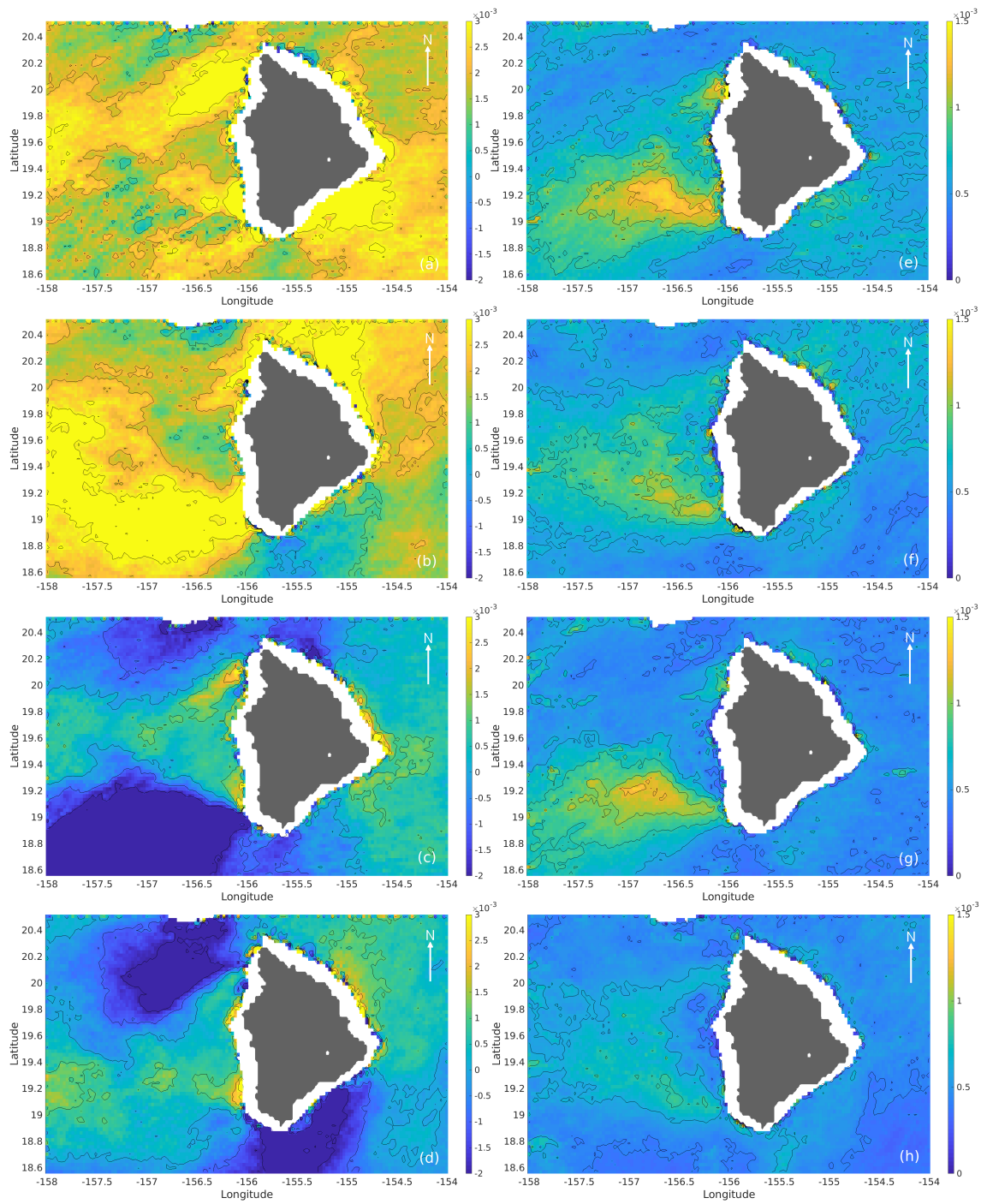
Figure 4.9: Panels (a)–(d) show the average difference in linear values between measured QuikSCAT σ^0 and predicted HRCM σ^0 for each flavor of σ^0. (e)–(h) show the standard deviation of the difference between measured QuikSCAT σ^0 and HRCM predicted σ^0 normalized by QuikSCAT average wind speeds in linear values. The first row shows values for VF, second is VA, third HF, and the fourth row is HA. The land is shown in gray and the land buffer is shown in white.

directions of the chosen north and south locations are similar but vary slightly in σ^0 due to χ. Error bars showing the average difference between ASCAT measured σ^0 and NWP predicted σ^0 and the standard deviation of the differences are in black. The top row of the figure shows the fore look, the middle row shows the mid look, and the bottom row shows the aft look.

Fig. 4.10 (d)–(f) show NWP predicted σ^0 taken from the same north and south pocket locations as the ASCAT measurements. In general the reported NWP wind speeds are much lower than that of ASCAT and fall on a σ^0 curve that does not vary much with χ. Comparing (a) and (d) shows that there is a greater difference between the ASCAT measured σ^0 and NWP predicted σ^0 at the north end. The σ^0 at the southern end have a relatively small difference, even though the wind speed and direction differences between ASCAT and NWP are similar at the north and south end. A similar comparison of (c) and (f) shows that there is a greater difference between σ^0 at the southern end and the difference at the northern end is relatively small. In the mid antenna look ((b) and (e)) both north and south points have close to the same difference in σ^0.

The change in differences is explained by a change in antenna azimuth look angle which effects χ. The differences in wind speed and direction may be the same for the two points but the azimuth angle can hide the differences in σ^0. This effect can be seen to varying degrees in Fig. 4.9 and in subsequent figures in this section. The high variability of HRCM winds makes it difficult to precisely identify this effect, but artifacts can still be seen.

Measured QuikSCAT σ^0 are compared with coarse NWP predicted σ^0. The coarse wind fields do not resolve the reverse flow wind features well (wind speed or direction) and are a good baseline comparison to see if the UHR σ^0 show the reverse flow features. Fig. 4.11 (a)–(d) shows the average difference between measured QuikSCAT σ^0 and QMOD3 NWP predicted σ^0. As expected, the average differences show that NWP is not modeling what QuikSCAT is detecting. There are large differences in the high wind speed pocket regions, especially for the vertical polarization. The horizontal polarization shows differences in the same areas but with smaller differences on average. This is consistent with the the QuikSCAT horizontal polarization being lower than the HRCM σ^0 seen in Fig. 4.9 (c) and (d). Both polarizations have a low average difference immediately west of the Big Island.

Fig. 4.11 (e)–(h) show the standard deviation of the differences for QuikSCAT and NWP σ^0 normalized by QuikSCAT average wind speeds. There are high standard deviation values
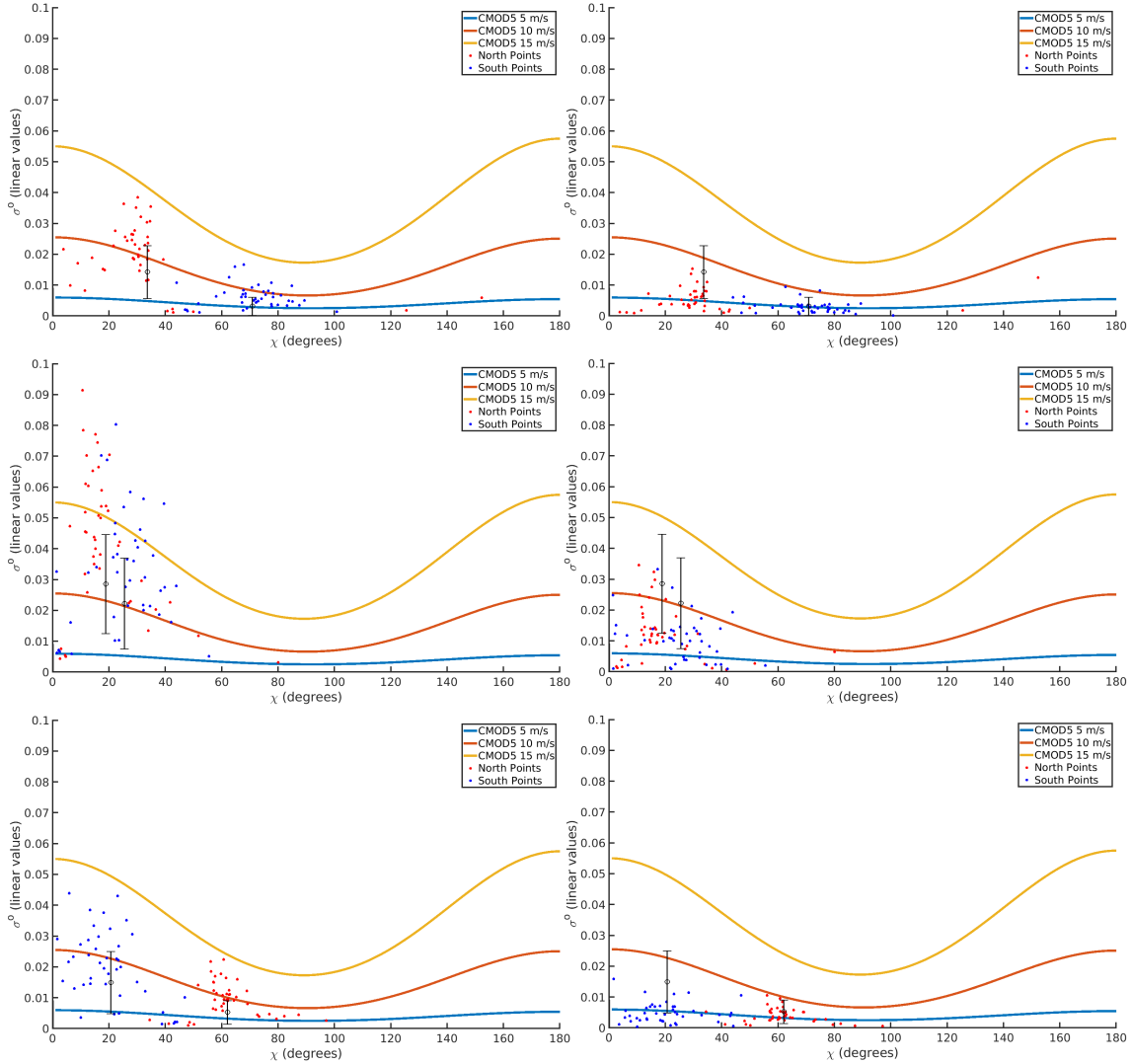
Figure 4.10: ASCAT σ^0 from multiple revs from a point in the north high wind speed pocket and a point in the south wind speed pocket are plotted for fore (a), mid (b), and aft (c) looks. Corresponding NWP predicted σ^0 are shown in (d)–(f). σ^0 curves at 50° incidence angle for CMOD5 for 5, 10, and 15 m/s are plotted in each panel for reference. Error bars showing the average difference between ASCAT measured σ^0 and NWP predicted σ^0 and the standard deviation of the differences are plotted in black.

(especially for vertical polarization) west of the island even in the area immediately behind the island where a reverse flow is expected. The disagreement between the mean flow dominated NWP and QuikSCAT σ^0 measurements further suggests that QuikSCAT σ^0 are possibly detecting a reverse flow and vortexes.

4.3.2 ASCAT Versus Predicted σ^0

The average difference between the ASCAT measured σ^0 and HRCM CMOD5 predicted σ^0 is shown in Fig. 4.12. The top row in Fig. 4.12 shows fore, the middle shows mid, and the bottom row shows aft beam looks. Average difference between the ASCAT σ^0 and HRCM σ^0 are shown in the left column and the standard deviation of the differences normalized by average ASCAT wind speeds are shown in the right column. In Fig. 4.12 a dividing line can be seen east of the where there is limited coverage from ASCAT passes. Data from that area can be ignored due to the limited amount of passes that covered that area.

Like the QuikSCAT comparison, larger differences can be seen in the high wind speed pocket areas. The effects of azimuth angle can be seen especially when comparing the fore and aft azimuth looks. Immediately west of the island the average differences and standard deviation values are low for all looks. This is interesting, because like QuikSCAT, ASCAT final selected wind directions do not show the reverse flow. The low average difference and low normalized standard deviation values west of the island suggest that ASCAT is detecting the reverse flow. The variance in differences in the high wind speed pocket areas suggest that the orientation of the wind speed tail and placement of vortexes by HRCM does not match what ASCAT σ^0 is detecting.

ASCAT measured σ^0 and NWP predicted σ^0 are compared in Fig. 4.13. The top row in Fig. 4.13 shows fore, the middle shows mid, and the bottom row shows aft beam looks. Average difference between the ASCAT σ^0 and NWP σ^0 are shown in the left column and the standard deviation of the differences normalized by average ASCAT wind speeds are shown in the right column. Like QuikSCAT, ASCAT σ^0 show high differences from NWP σ^0 in the high wind speed pocket regions and low differences immediately west of the island. The standard deviation plots show that the reverse flow features that ASCAT σ^0 is detecting vary. The variation seen immediately west of the island suggests that ASCAT σ^0 can be detecting something other than the mean flow in that region.
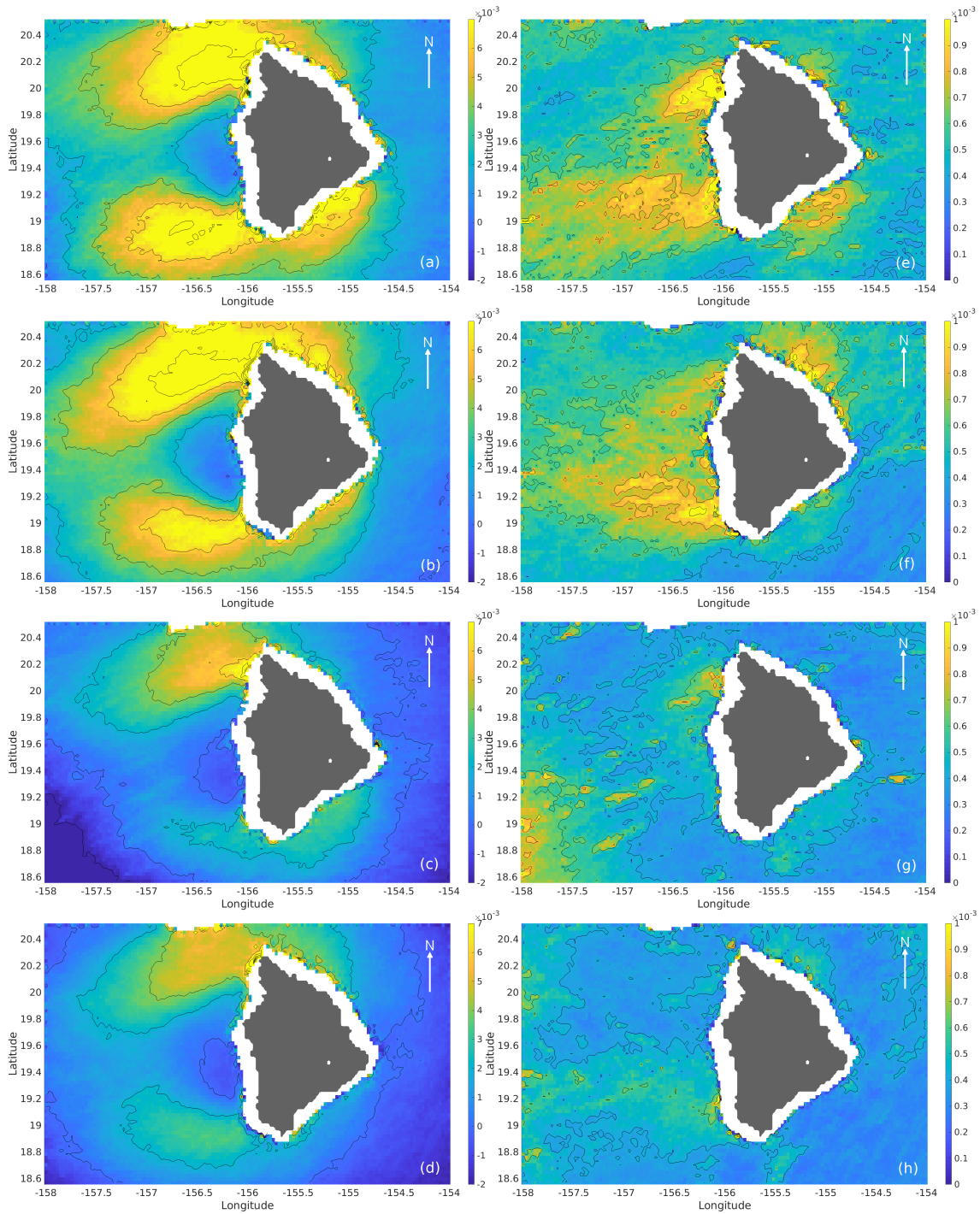
Figure 4.11: Panels (a)–(d) show the average difference in linear values between measured QuikSCAT σ^0 and NWP predicted σ^0 for different flavors of σ^0. (e)–(h) show the normalized standard deviation in linear values between measured QuikSCAT σ^0 and NWP predicted σ^0. The first row is VF, second is VA, third HF, and the fourth row HA. The land is shown in gray and the land buffer is shown in white.
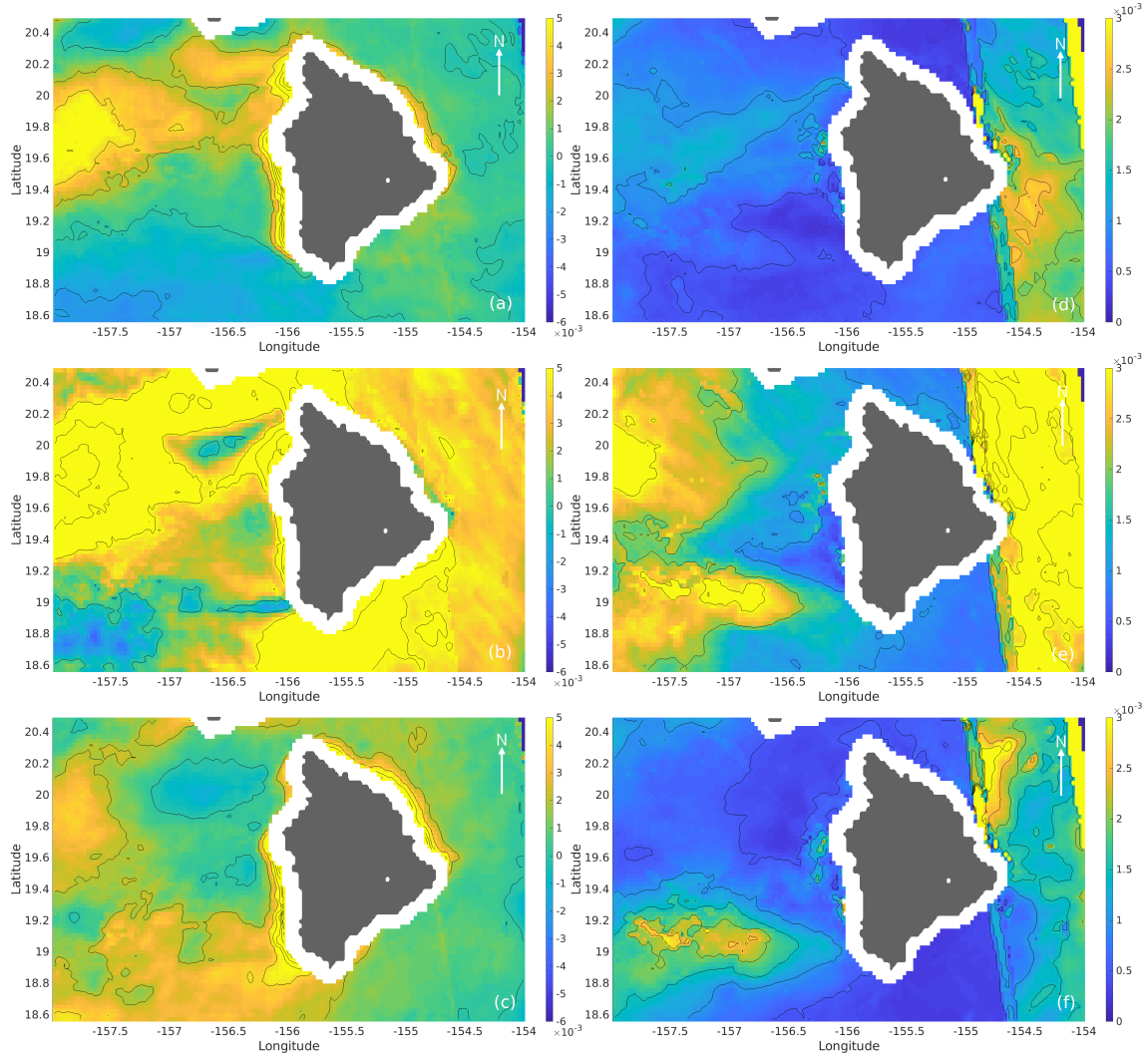
Figure 4.12: The average difference between linear values of measured ASCAT σ^0 and HRCM predicted σ^0 shown for fore (a), mid (b), and aft (c) beams. Corresponding normalized standard deviation of the difference values are shown to the right in panels (d)–(f). The land is shown in gray and the land buffer is shown in white.

4.3.3 Average Wind Speeds

The average wind speeds for all the data sets are a useful tool in analyzing the σ^0 comparisons. Average wind speeds from the selected passes for the σ^0 comparison above are shown in Figs 4.14 and 4.15. Fig. 4.14 shows QuikSCAT (a), HRCM (b), and NWP (c) average wind speeds. Average QuikSCAT wind speeds in the high wind speed pocket area are lower than the HRCM predicted speeds. QuikSCAT wind speeds show a much shorter low wind speed tail than HRCM winds. The NWP winds do not resolve any of the reverse flow speed features well.
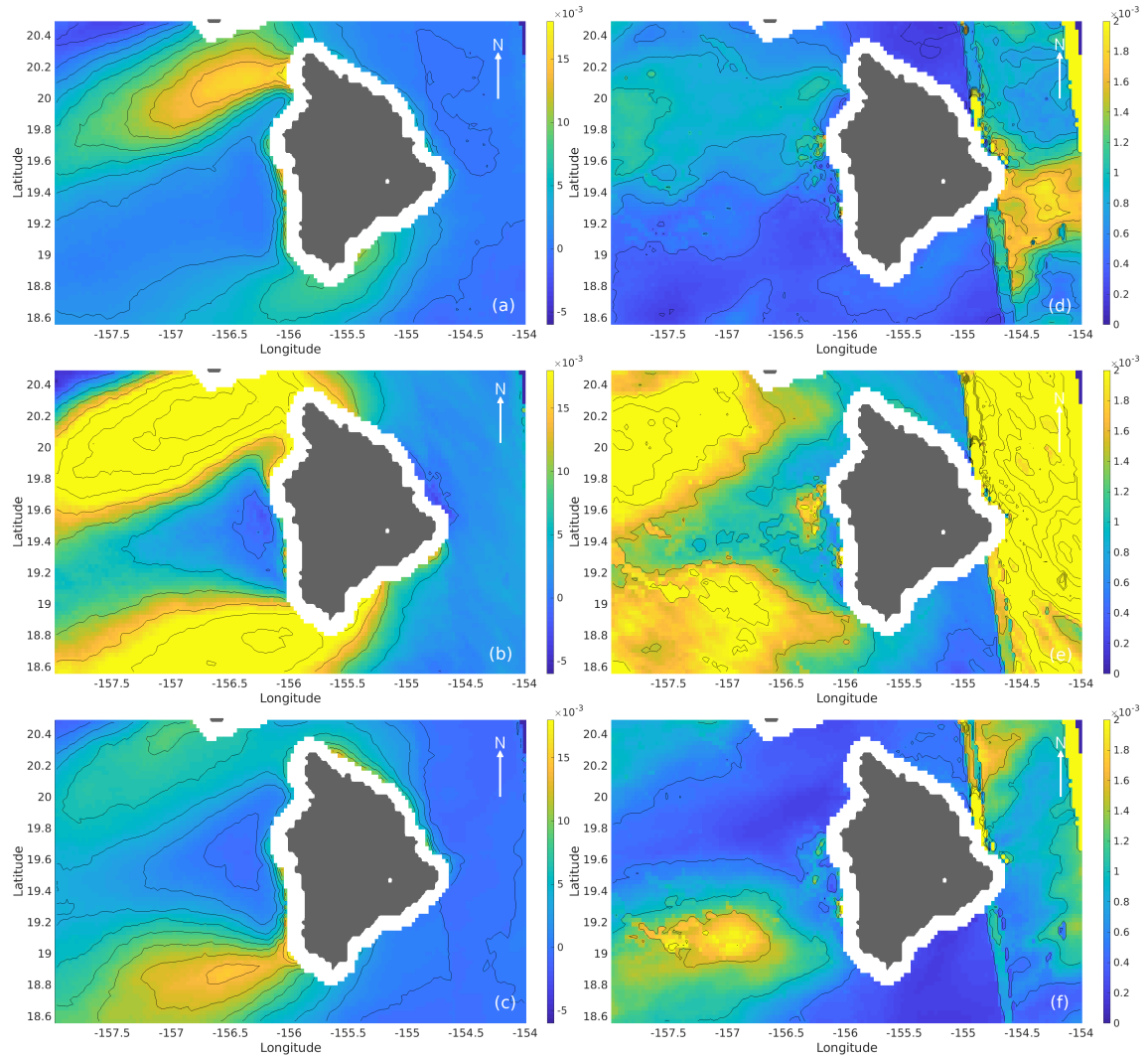
Figure 4.13: The average difference between linear values of measured ASCAT σ^0 and NWP predicted σ^0 shown for fore (a), mid (b), and aft (c) beams. Corresponding normalized standard deviation of the difference values are shown to the right in panels (d)–(f). The land is shown in gray and the land buffer is shown in white.

Fig. 4.15 shows ASCAT (a), HRCM (b), and NWP (c) average wind speeds. The ASCAT low wind speed tail is narrower than that shown in the HRCM winds. On average, ASCAT resolves a longer tail than QuikSCAT. The northern ASCAT high wind speed pocket area is larger than that shown in HRCM. NWP wind speeds poorly resolve most wind speed features in the lee of the island.
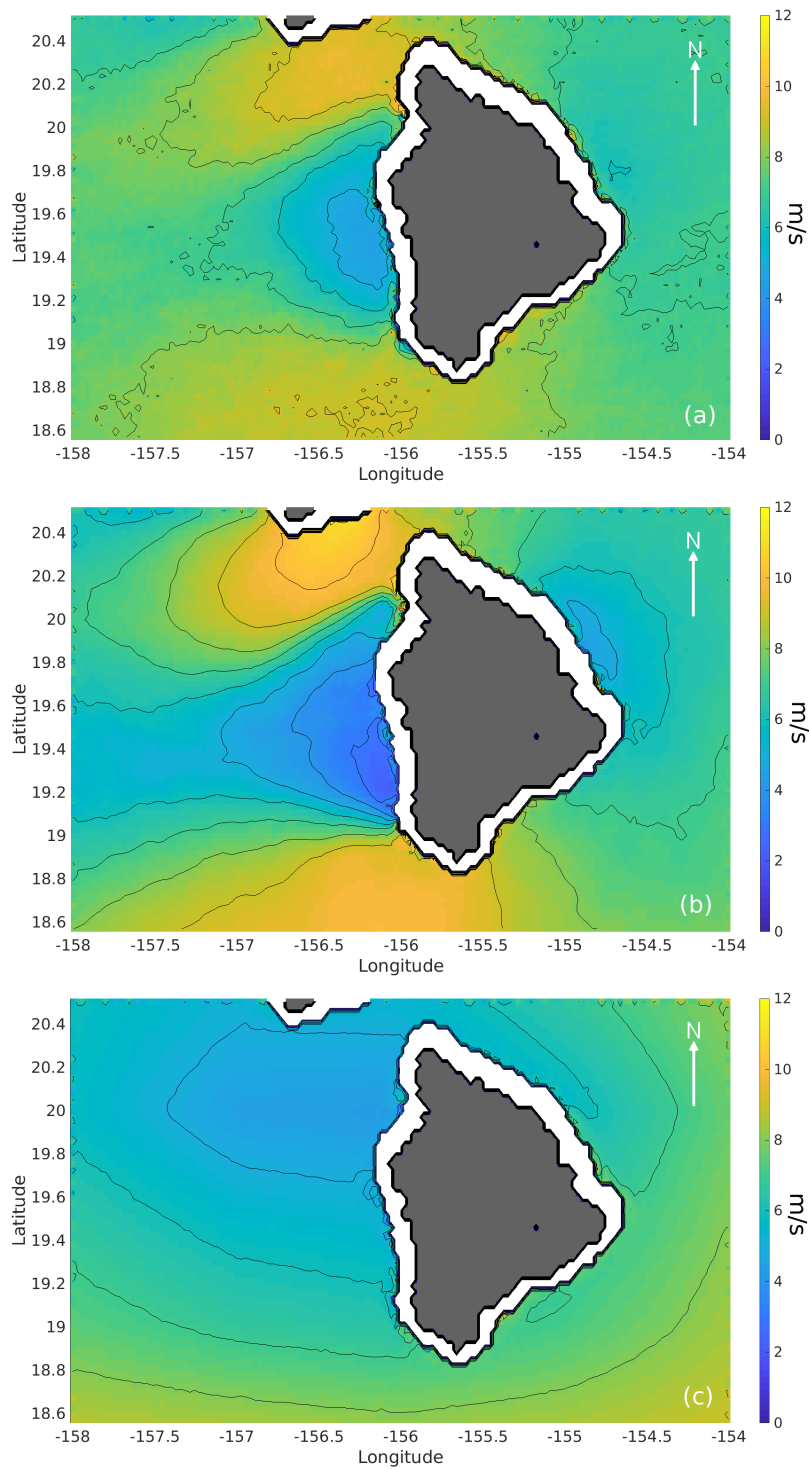
Figure 4.14: Average wind speeds around the Big Island for QuikSCAT (a), collocated HRCM (b), and NWP (c). The average is over the collocated wind fields used in the σ^0 analysis. A land mask is shown in gray with the land buffer shown in white.
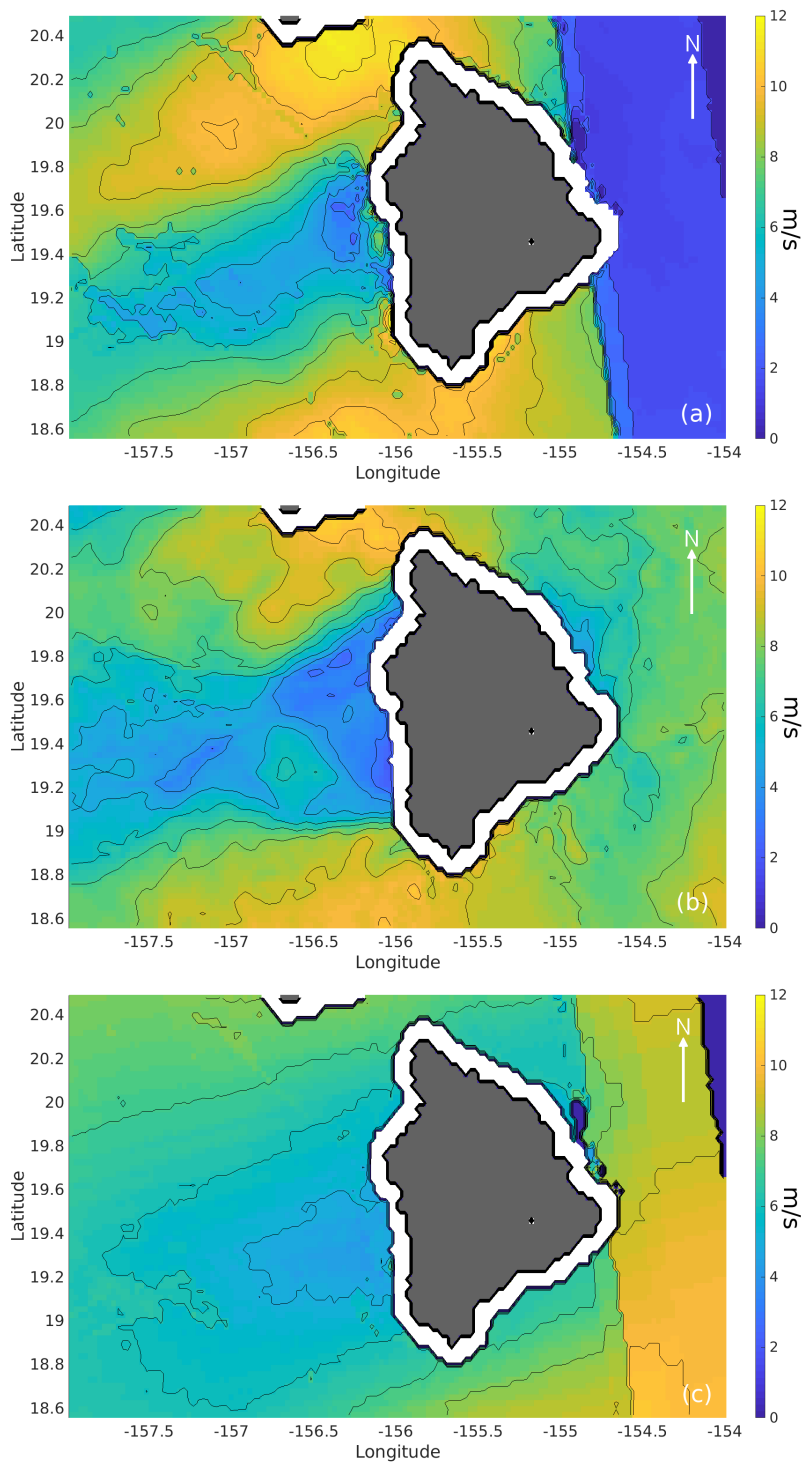
Figure 4.15: Average wind speeds around the Big Island for ASCAT (a), collocated HRCM (b), and NWP (c). The average is over the collocated wind fields used in the σ^0 analysis. A land mask is shown in gray with the land buffer shown in white.

4.3.4 Summary

Average difference and normalized standard deviation plots from both scatterometers indicate that the HRCM features do not match the scatterometer σ^0 measured features. However, comparison with the coarse NWP winds show that UHR σ^0 from both sensors do detect reverse flow features. Low differences and low standard deviation values compared to HRCM predicted σ^0 immediately west of the island suggest that the scatterometer σ^0 is consistent with the reverse flow. The variation seen when compared to the NWP σ^0 further supports the idea that the scatterometer σ^0 can be detecting the island induced perturbation of the mean flow. Higher standard deviation values in the HRCM comparisons in the high wind speed pocket areas suggest that HRCM is misplacing key wind features. The following section details why the final selected wind fields may not show the wind features even if they are detected in the σ^0.

4.4 Nudging Field and Median Filter Window Size

The nudging field and median filter-based ambiguity selection scheme have a significant effect on the final selected scatterometer wind field. They ensure general wind trends are present, but also smooth the final result. [33] identifies the difficulties that the nudging field and introduce to wind retrieval in this area for coarse resolution wind estimates. In this section, I explore the effects of the nudge winds and median filter window size on UHR estimates.

I employ simulation to explore the effects of the nudging field and median filter window size on UHR wind estimation in the lee of the Big Island. σ^0 measurements are generated using an HRCM wind field as input. Simulated σ^0 measurements are created from HRCM winds using the QMOD3 GMF and the satellite footprint is treated as non-uniform. Non-uniform means that the each σ^0 measurement represents the weighted average surrounding WVCs that the footprint covers. Non-uniform and uniform footprints yield similar results in this region. Monte Carlo noise is also added to the σ^0 measurements. The simulation uses real satellite geometry from an actual pass, so each point has a realistic, unique measurement geometry. The noisy σ^0 measurements are then processed using traditional QuikSCAT UHR processing. Among the ambiguous solutions are wind speed and direction values that are close to the true model values. I chose to focus on QuikSCAT for this simulation; however, ASCAT yields similar results.

I first examine the effects of the nudging field. Traditional QuikSCAT UHR wind estimation uses L2B wind fields as a nudging fields and L2B is nudged with NWP wind fields. Consequently, UHR is indirectly nudged with coarse 50 km NWP model winds. Fig. 4.16 (a) is a simulated HRCM wind field nudged with an L2B wind field and (c) shows the simulated field nudged with the "truth" (the original HRCM wind field). For clarity, downsampled wind direction quivers are plotted in all panels. In both (a) and (c) the low wind speed tail and high wind speed pockets are resolved. There is a similarity in wind speed between (a) and (c) because the nudging field affects the wind direction more than it does the wind speed. The wind speeds in a single WVC do not vary much from ambiguity to ambiguity, while direction can vary drastically. Where we expect the directions in (a) to show the reverse flow, there are no reverse flow features. Comparing (a) and (c) reveals that the ambiguities of the WVCs in lee of the Big Island can represent the reverse flow feature, the difference being the nudging field. Thus, (a) shows that key features can be misrepresented or absent if the nudging field is low resolution.

After the ambiguous field is nudged, it is processed with the median filter-based ambiguity selection scheme. As mentioned earlier, a median filter is chosen because it reduces noise and preserves wind fronts. Fig. 4.16 (b) is the L2B nudged field that has been median filtered with a 42.5 km (17 x 17 UHR WVC) window. Fig. 4.16 (d) shows the truth nudged field median filtered with the same window. The main wind direction features (i.e., trade wind flow and/or reverse flow) in (a) and (c) are preserved in (b) and (d) respectively. The median filtered field in (a) does not show the reverse flow because it was not there to begin with. The filter can only preserve and refine what is already there. The reverse flow in (b) is preserved in (d) after the median filter.

The median filter window size affects how well features are resolved. If the median filter window is large, small features relative to the window can be lost. Fig. 4.17 shows Fig. 4.16 panels (c) and (d) but in a swath oriented gray scale wind direction field to better illustrate this point. Fig. 4.17 (a) shows the truth nudged field before filtering. Note the reverse flow in the lee of the Big Island and wind features near the other islands (boxed in red). Fig. 4.17 (b) shows the field after filtering with the same 42.5 km window. The relatively large reverse flow from (a) is still present in (b), but the smaller features near the other islands are filtered away. These results confirm that the median filter can preserve the reverse flow feature only if the feature is in the nudging field to begin with and the window size is not too large relative to the feature.

58
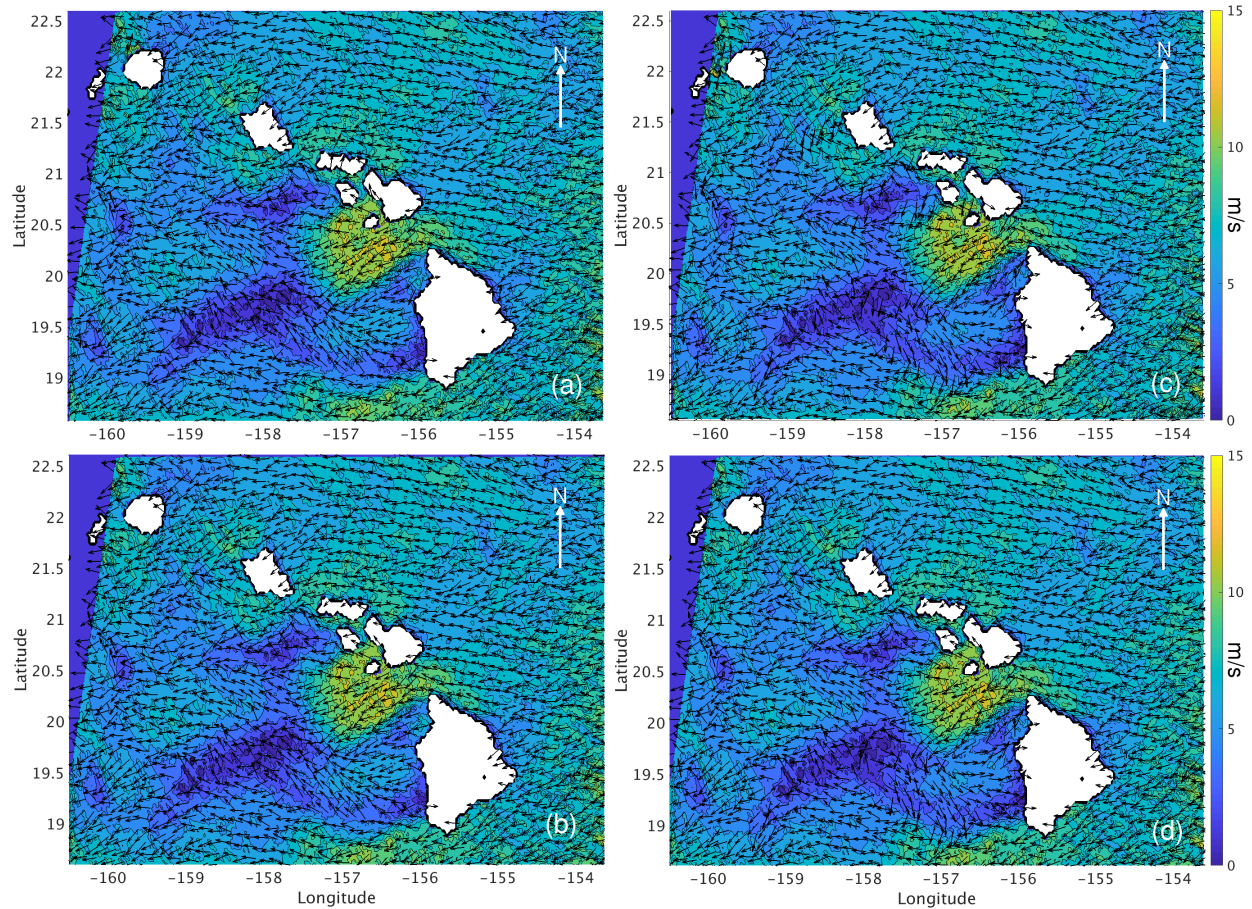
Figure 4.16: Simulated HRCM wind field nudged with an L2B field (a), simulated field nudged with L2B and median filtered (b), simulated field nudged with the true field (c), simulated field nudged with true field and median filtered (d). The median filter window size is 42.5 km (17 x 17 UHR WVC).

4.5   Conclusion

QuikSCAT and ASCAT L2B and UHR processing have been proven to provide accurate estimates of ocean wind vectors over open ocean regions. The lee of the Big Island of Hawaii presents an interesting case where wind retrieval for L2B or UHR (for both sensors) does not resolve the complex wind features in the final selected wind fields compared to HRCM winds. However, comparison of measured σ^0 to HRCM predicted σ^0 show that the scatterometer σ^0 can be detecting reverse flow features. Scatterometer σ^0 compared with NWP σ^0 that represent only the mean flow shows that the scatterometer σ^0 are detecting disturbances in the mean wind flow. The reverse flow features are likely missing in the final selected wind field due to coarse nudging
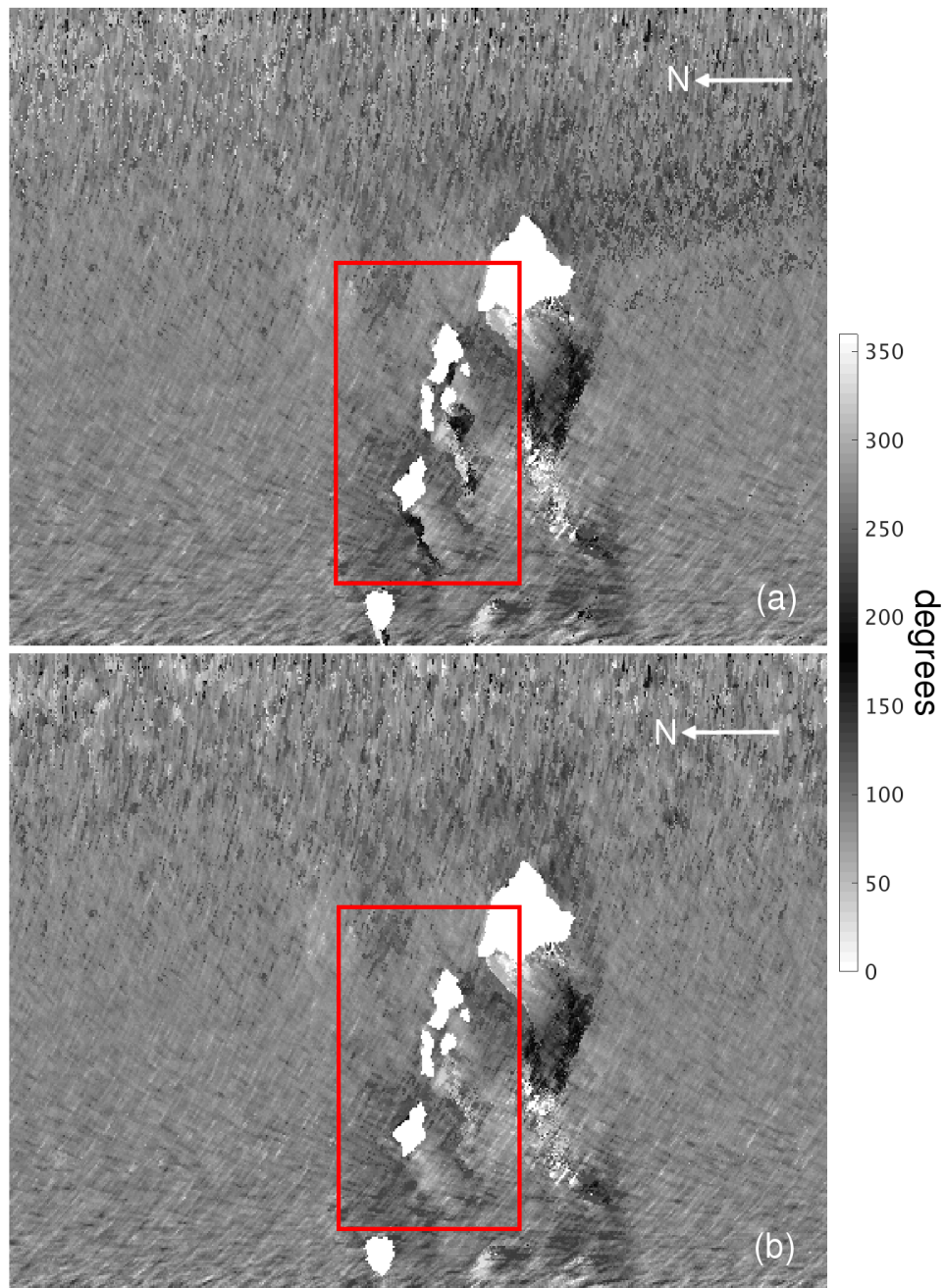
Figure 4.17: QuikSCAT UHR-derived wind direction fields for different median filter window sizes. (a) shows a swath oriented wind direction field of a simulated HRCM wind field nudged with the true wind field. (b) shows (a) smoothed with a 42.5 km (17 x 17 UHR WVC) median filter window. Note how the features different from the mean flow in the red box in (a) disappear in (b) after filtering. The land mask is shown in white and the colorbar denotes the wind direction in degrees.

fields and a large window size for the median filter. Additionally, the σ^0 analysis indicates that HRCM winds are inaccurately predicting the locations of key reverse flow features compared to the scatterometer σ^0. It is thought that, incorporating high resolution scatterometer data into the HRCM could result in better wind prediction. To improve UHR wind retrieval in this area, a better representation of fine scale features near Hawaii is needed.

CHAPTER 5.   CONCLUSION

5.1   Summary

This thesis explores UHR wind estimates from multiple sensors in different near coastal regions. Chapter 1 introduces the sensors used in this thesis and motivates UHR scatterometry. Chapter 2 provides necessary background information on different scatterometer architectures, explains wind estimation, and describes current scatterometer limitations. Chapter 3 introduces and validates RapidScat UHR wind estimates with offshore buoys near the east coast of the United States. It also shows that RapidScat wind retrieval improves with the addition of DIR and AA to the wind processing algorithm. DIR and AA reduce RMS difference from NWP winds across the swath.

Chapter 4 compares QuikSCAT and ASCAT data in the lee of Hawaii's Big Island with high resolution model winds. First the wind speeds and directions of the sensors are compared with the model winds. The comparison shows that neither sensor at L2B or UHR resolution is able to resolve reverse flow wind direction features. Scatterometer wind speeds only partially resolve reverse flow wind speed features compared to HRCM winds. Scatterometer measured σ^0 are compared to NWP and HRCM predicted σ^0. The σ^0 analysis suggests that the scatterometer σ^0 is detecting the reverse flow. Differences between scatterometer σ^0 and HRCM predicted σ^0 suggest that the model is incorrectly placing key reverse flow features. The reverse flow features likely do not show up in the final selected wind field because of coarse nudging fields and a large median filter window size.

5.2   Contributions

The contributions of this thesis to the field of UHR scatterometry are listed below:

• Validation of Near-Coastal RapidScat UHR Wind Estimates

Traditionally processed RapidScat UHR wind estimates are introduced and compared to offshore buoys near the east coast of the United States. UHR estimates are noisier than the coarser L2B wind estimates, but still match well with the buoy wind measurements. UHR wind speed estimates have greater noise at low wind speeds than L2B estimates. UHR wind directions match the measured buoy directions well at all wind speeds. This comparison shows the feasibility of UHR RapidScat wind estimates.

- Validation and Application of DIR with AA to UHR RapidScat Wind Retrieval

DIR has been applied previously to both coarse and fine resolution wind retrieval in many scatterometers. In this thesis, DIR is applied to RapidScat UHR wind retrieval. Additionally, AA are added into the wind retrieval process to ameliorate the effect of WVCs with a single ambiguity. Wind vectors retrieved with DIR and AA are validated in near-coastal regions against ocean buoys. The new algorithm shows less noise in wind direction and decreases RMS error across the swath compared to traditionally processed wind estimates. Near-nadir wind estimates have a significant decrease in RMS error.

- Optimal Median Filter Window Size for RapidScat UHR Estimates

The optimal median filter window size for the median filter-based ambiguity selection scheme is determined by considering computation time and RMS difference from NWP winds. The chosen window size reduces RMS difference from model winds, preserves high resolution features in the east coast area, and consumes a reasonable amount of computation time.

- Comparison of L2B and UHR Scatterometer Winds with HRCM Predicted Winds Near Hawaii

Scatterometer wind estimates from QuikSCAT and ASCAT are compared against HRCM winds in the lee of Hawaii's Big Island. L2B wind estimates from both QuikSCAT and ASCAT do not resolve well the features expected in that region. The L2B directions lack the reverse flow and vortexes that the HRCM models show. UHR winds from both sensors better resolve some features but still are not sufficient compared to the model. UHR wind estimates show the expected low wind speed tail and high wind speed pockets. However, the fine resolution wind direction features (the vortexes and reverse flow) are absent. The scatterometer wind fields are dominated by the trade

wind flow when we expect to see other features. Comparison of the scatterometer winds and the model winds exposes a limitation of the scatterometer wind estimation in near-coastal mountain regions.

- Comparison of Measured σ^0 to Predicted Model σ^0 Near Hawaii

Using QuikSCAT's QMOD3 and ASCAT's CMOD5, predicted HRCM and NWP σ^0 are generated for comparison with scatterometer measured σ^0. Scatterometer σ^0 compared the HRCM σ^0 have a low average difference and a low standard deviation immediately behind the island. This suggests that the scatterometer σ^0 can be detecting the reverse flow. Variation in the high wind speed pocket areas indicate that HRCM is incorrectly placing key wind features behind the island compared to the scatterometer measurements. Higher normalized standard deviation values west of the island when compared to NWP σ^0 suggest that the scatterometer σ^0 can be detecting the disturbances in the mean wind flow caused by the island.

- Effect of Coarse Nudging Fields and Fixed Median Filter Window Size

Coarse nudging fields and a fixed size median filter window are shown to greatly affect the ability to resolve fine resolution wind features. Ambiguous solutions in scatterometer wind retrieval necessitates the use of outside data sets to ensure accurate wind flow. A lack of truth data means that coarse NWP are used to nudge ambiguous scatterometer wind fields. The coarse nudging fields can hide fine resolution features in the scatterometer wind field. I also show that a median filter window that is too large can smooth away fine resolution features. This analysis shows limitations of current wind UHR processing techniques and shows that the nudging field and median filter-based ambiguity selection scheme window size may be why the reverse flow features are absent in the final selected wind field. To improve UHR wind retrieval in this area, a better representation of fine scale features near Hawaii is needed and an optimum window size needs to be found.

- New Wind Model for QuikSCAT in the Near Hawaii Area

Appendix A outlines the creation of a GMF specific to the near Hawaii region using HRCM winds and QuikSCAT measured backscatter. Unfortunately, the new GMF does not improve

QuikSCAT wind retrieval in that area. In wind fields processed with the new model, wind speed values are pushed to the extremes (very low or very high) and wind directions are dominated by noise. This experiment shows the robustness of QMOD3 but does not mean that a new model could not work for other scatterometers.

5.3 Future Work

The following related topics can be pursued further:

- Incorporate UHR Winds into HRCM Models

HRCM winds show the expected reverse flow features in the lee of the Big Island. However, differences in HRCM simulated σ^0 and scatterometer measured σ^0 indicate some error in the model. The HRCM uses coarse 25 km QuikSCAT wind speeds among other data sets as an input. UHR scatterometer data could be used to improve HRCM accuracy. The finer resolution data could fine tune the wind speed features and vortex locations that HRCM predicts.

- Explore UHR Ambiguity Selection the Near Hawaii Area

This thesis showed the importance of an accurate nudging field and the effect that the median filter-based ambiguity selection scheme has on fine resolution features. Further work could be done on finding a more suitable nudging field or another approach to ambiguity initialization in the near Hawaii area. If UHR winds were incorporated into the HRCM, the model winds would be an excellent candidate to nudge the fields. Synthetic wind fields could also potentially be used to see if vortexes are resolved in the ambiguities. After solving the initialization step, work must be done to find the optimal median filter window size for this area. The window must be chosen to preserve features and smooth the field.

- ASCAT σ^0 Comparison on a Larger Data Set

ASCAT collocations near the hour (HRCM winds are given hourly on the hour) are less common than QuikSCAT. More years of data would provide a more robust σ^0 comparison. A comparison of both left and right swaths and other incidence angles could be done with more orbits. This comparison could give more insight into whether ASCAT σ^0 are detecting reverse flow features.

- Explore a Regional GMF for ASCAT

In Appendix A a GMF for QuikSCAT specific to the near Hawaii area is created. Unfortunately, the near Hawaii GMF does not improve QuikSCAT wind retrieval in that area. ASCAT has different geometry and backscatter than that of QuikSCAT. A specialized GMF for ASCAT in that area could improve wind retrieval in the near Hawaii area.

- Explore UHR Capabilities Near the California Bight

QuikSCAT and ASCAT 12.5 km grid resolution products have systematic errors near the California Bight [33]. UHR wind products could better resolve the features expected in that region. A similar study to the one done in this thesis could be done in that region.

REFERENCES

[1] F. T. Ulaby and D. G. Long, *Microwave Radar and Radiometric Remote Sensing*. The University of Michigan Press, 2014. vi, 1, 5, 6, 7

[2] National Data Buoy Center, June 2018. [Online]. Available: http://www.ndbc.noaa.gov vi, 11, 12

[3] P. S. Chang, Z. Jelenak, J. M. Sienkiewicz, R. Knabb, M. J. Brennan, and D. G. Long, "Operational use and impact of satellite remotely sensed ocean surface vector winds in the marine warning and forecasting environment," *Oceanography*, vol. 22, no. 2, pp. 194–207, 2009. 1, 5

[4] D. G. Long, "Polar applications of spaceborne scatterometers," *IEEE Journal of Selected Topics in Applied Earth Observations*, vol. 10, no. 3, pp. 2307–2320, 2017. 1

[5] D. B. Lindell and D. G. Long, "High-resolution soil moisture retrieval with ASCAT," *IEEE Geoscience and Remote Sensing Letters*, vol. 13, no. 7, pp. 972–976, 2016. 1

[6] D. Lindell and D. Long, "Multiyear arctic ice classification using ASCAT and SSMIS," *Remote Sensing*, vol. 8, no. 4, p. 294, 2016. 1

[7] B. A. Williams, M. P. Owen, and D. G. Long, "The ultra high resolution QuikSCAT product," *2009 IEEE Radar Conference*, pp. 1–6, May 2009. 1, 11

[8] A. Plagge, D. C. Vandemark, and D. G. Long, "Coastal validation of ultra-high resolution wind vector retrieval from QuikSCAT in the Gulf of Maine," *IEEE Geoscience and Remote Sensing Letters*, vol. 6, no. 3, pp. 413–417, 2009. 1, 2, 11

[9] R. D. Lindsley, "Enhanced-Resolution Processing and Applications of the ASCAT Scatterometer," Ph.D. dissertation, Brigham Young University, 2015. 1, 2, 9, 11, 40

[10] N. Hutchings and D. G. Long, "Improved ultrahigh-resolution wind retrieval for RapidScat," *IEEE Transactions on Geoscience and Remote Sensing*, vol. 57, no. 6, pp. 3370–3379, 2018. 1

[11] S. L. Durden and D. Perkovic-Martin, "The RapidScat ocean winds scatterometer," *IEEE Transactions on Geoscience and Remote Sensing*, vol. 5, no. 3, pp. 36–41, 2017. 1, 2, 13

[12] J. Yang and J. Zhang, "Evaluation of ISS-RapidScat wind vectors using buoys and ASCAT data," *Remote Sensing*, vol. 10, no. 4, p. 648, 2018. 2, 35

[13] N. Ebuchi, "Evaluation of marine vector winds observed by RapidScat on the International Space Station using statistical distribution," in *Geoscience and Remote Sensing Symposium (IGARSS), 2015 IEEE International*. IEEE, 2015, pp. 4901–4904. 2

[14] Physical Oceanography Distributed Active Archive Center (PO.DAAC), "Seawind's user guide," vol. 3.0, no. D-18053, June 2006. 2, 6, 46, 73

[15] B. A. Williams and D. G. Long, "A reconstruction approach to scatterometer wind vector field retrieval," *IEEE Transactions on Geoscience and Remote Sensing*, vol. 49, no. 6, pp. 1850–1864, 2011. 2

[16] M. W. Spencer, W.-T. Tsai, and D. G. Long, "High resolution measurements with a spaceborne pencil-beam scatterometer using combined range/Doppler techniques," *IEEE Transactions on Geoscience and Remote Sensing*, vol. 41, no. 3, pp. 567–581, 2003. 2

[17] J. Figa-Saldaña, J. J. Wilson, E. Attema, R. Gelsthorpe, M. Drinkwater, and A. Stoffelen, "The advanced scatterometer (ASCAT) on the meteorological operational (MetOp) platform: A follow on for European wind scatterometers," *Canadian Journal of Remote Sensing*, vol. 28, no. 3, pp. 404–412, 2002. 2

[18] Ocean and Sea Ice SAF Team, "ASCAT wind product user manual," Royal Netherlands Meteorological Institute, Tech. Rep., 03 2016. 2, 5

[19] R. Lindsley and D. G. Long, "Enhanced-resolution reconstruction of ASCAT backscatter measurements," *IEEE Transactions on Geoscience and Remote Sensing*, vol. 54, no. 5, pp. 2589–2601, 2016. 2

[20] W. T. Liu and W. Tang, "Equivalent neutral wind," Unpublished Paper, 1996. 6, 11, 73

[21] B. W. Stiles, B. D. Pollard, and R. S. Dunbar, "Direction interval retrieval with thresholded nudging: a method for improving the accuracy of QuikSCAT winds," *Transactions of Geoscience and Remote Sensing*, vol. 40, no. 1, pp. 79–89, 2002. 7, 8, 19, 20

[22] F. M. Naderi, M. H. Freilich, and D. G. Long, "Spaceborne radar measurement of wind velocity over the ocean-an overview of the NSCAT scatterometer system," *Proceedings of the IEEE*, vol. 79, no. 6, pp. 850–866, 1991. 7, 73

[23] S. J. Shaffer, R. S. Dunbar, S. V. Hsiao, and D. G. Long, "A median-filter-based ambiguity removal algorithm for NSCAT," *IEEE Transactions on Geoscience and Remote Sensing*, vol. 29, no. 1, pp. 167–174, 1991. 7, 8, 16

[24] H. Schultz, "A circular median filter approach for resolving directional ambiguities in wind fields retrieved from spaceborne scatterometer data," *Journal of Geophysical Research*, vol. 95, no. C4, pp. 5291–5303, 1990. 7, 16

[25] M. H. Freilich and R. S. Dunbar, "The accuracy of the NSCAT 1 vector winds: comparisons with National Data Buoy Center buoys," *Journal of Geophysical Research*, vol. 104, no. C5, pp. 11 232–11 246, 1999. 12, 13, 36, 38

[26] J. C. Russ, *The Image Processing Handbook*. CRC Press Inc., 1995. 16

[27] E. C. Nickerson and M. A. Dias, "On the existence of atmospheric vortices downwind of hawaii during the hamec project," *Journal of Applied Meteorology*, vol. 20, no. 8, pp. 868–873, 1981. 35

[28] R. B. Smith and V. Grubišić, "Aerial observations of Hawaii's wake," *Journal of the Atmospheric Sciences*, vol. 50, no. 22, pp. 3728–3750, 1993. 35

[29] W. C. Patzert, "Eddies in hawaiian waters," Hawaii Inst of Geophysics Honolulu, Tech. Rep., 1969. 35

[30] C. Zhang, A. L. Yuqing Wang, and K. Hamilton, "Configuration and evaluation of the WRF model for the study of Hawaiian regional climate," *American Meteorological Society*, vol. 140, pp. 3259–3277, 2012. 35

[31] Asia-Pacific Data Research Center, January 2019. [Online]. Available: http://apdrc.soest. hawaii.edu 35

[32] C. Zhang, Y. Wang, K. Hamilton, and A. Lauer, "Dynamical downscaling of the climate for the Hawaiian Islands. part i: Present day," *Journal of Climate*, vol. 29, no. 8, pp. 3027–3048, 2016. 35

[33] T. Kilpatrick, S.-P. Xie, H. Tokinaga, D. Long, and N. Hutchings, "Systematic scatterometer wind errors near coastal mountains," *Earth and Space Science*, Accepted 2019. 35, 36, 57, 67

[34] H. Hersbach, A. Stoffelen, and S. de Haan, "An improved c-band scatterometer ocean geophysical model function: CMOD5," *Journal of Geophysical Research: Oceans*, vol. 112, no. C3, 2007. 46, 73

[35] L. Ricciardulli and F. J. Wentz, "A scatterometer geophysical model function for climate-quality winds: QuikSCAT Ku-2011," *Journal of Atmospheric and Oceanic Technology*, vol. 32, no. 10, pp. 1829–1846, 2015. 73

APPENDIX A.

A GMF is an empirically derived relationship between the measured σ^0 and wind speed and direction [22]. The relationship is based on global wind and backscatter statistics [14]. Over the years many scatterometers have had their GMFs improved with the advent of better technology and new sensors [34, 35]. In this appendix I create a GMF specifically tuned for use near the Hawaiian islands.

For the analysis in Chapter 4, QuikSCAT's QMOD3 GMF was used. QMOD3, like most GMFs, is defined for 10 m equivalent neutral stability winds where the wind and wave fields are in equilibrium [20]. The Hawaiian islands study presents a unique case for QuikSCAT wind retrieval since the conditions that QMOD3 assumes do not always apply. The RF region contains a host of variable wind directions at a number of different wind speeds over short fetches. Unlike the open ocean, in the lee of the Big Island waves may not be able to develop enough. The underdeveloped waves could result in a σ^0 and wind velocity relationship inconsistent with the one that QMOD3 is based on. This inconsistency could negatively affect wind retrieval in the near Hawaii area.

Using QMOD3 in wind retrieval resolves the low wind speed tail and high wind speed pockets, but current wind retrieval techniques do not resolve any vortexes. A specialized near Hawaii GMF (NHGMF) could improve the retrieved wind directions and still resolve the wind speed features. Section A.1 describes how the NHGMF is made and Section A.2 outlines the results.

A.1 NHGMF

The NHGMF is created using measured σ^0 from QuikSCAT and HRCM wind vectors. HRCM wind vectors are considered truth for the purpose of this experiment (even if they may not be perfect). If we create a wind model using near Hawaii measured σ^0 and HRCM winds that show the expected RF features, we hope to see an improvement in the near Hawaii area.

73

A total of 548 QuikSCAT passes from 2003 to 2006 and corresponding HRCM winds are used to create the NHGMF. Only the area immediately around the Big Island (same as in Fig 4.4) and passes with the trade winds blowing from the northeast are considered. Focusing the Big Island area and on a certain trade wind flow ensures there is some consistency in the winds (i.e., the RF region is always to the west of the Big Island). Fortunately, the RF region provides a variety of wind speeds and directions which is crucial to an accurate GMF.

The NHGMF is created by first sorting σ^0 measurements in the area of interest by their collocated wind speed, azimuth angle, and polarization. The look angles and polarization come from the QuikSCAT passes and the wind speed and direction come from the HRCM models. The measurements are grouped into 1 m/s wind speed, 2° azimuth, and polarization bins. The σ^0 measurements in each bin are then averaged. Finally, the averaged σ^0 are smoothed with a spatial gaussian filter. The NHGMF does not span the entire range of speeds typically found in a GMF, so any gaps are filled in with QMOD3.

Fig A.1 shows the original NHGMF (a) and gaussian smoothed NHGMF (b) for the vertical polarization. The range of wind speeds shown is 1–15 m/s and 0°–90° azimuth angles. Fig. A.2 shows the original NHGMF (a) and the gaussian smoothed NHGMF (b) for the horizontal polarization over the same range. Figs A.3 and A.4 show the difference between NHGMF and QMOD3 for vertical and horizontal polarizations respectively. In both figures there is a large positive difference at low wind speeds, meaning that the NHGMF is larger in that area than QMOD3. This is due to the fact that at low wind speeds QuikSCAT UHR wind speeds estimates are generally higher than HRCM wind speeds. The measured σ^0 that previously related to a higher wind speed (QuikSCAT) are now mapped to a low one (HRCM). Thus, the NHGMF has higher σ^0 at lower wind speeds.

A.2   Results

The NHGMF is used in QuikSCAT UHR wind processing for multiple passes. The original QuikSCAT measured σ^0 are processed using the NHGMF. Unfortunately, by comparison to the original QMOD3 processed fields, the resulting fields do not show significant improvement. The wind directions, where I hoped to see the most improvement, are dominated by noise. Additionally, the extreme values in the wind speed field are more pronounced. That is the low wind speeds got

lower and the high wind speeds increased significantly. The extreme values in wind speed are likely explained by the large difference at low wind speeds between the two GMFs. We conclude that the NHGMF does not improve wind retrieval near Hawaii.
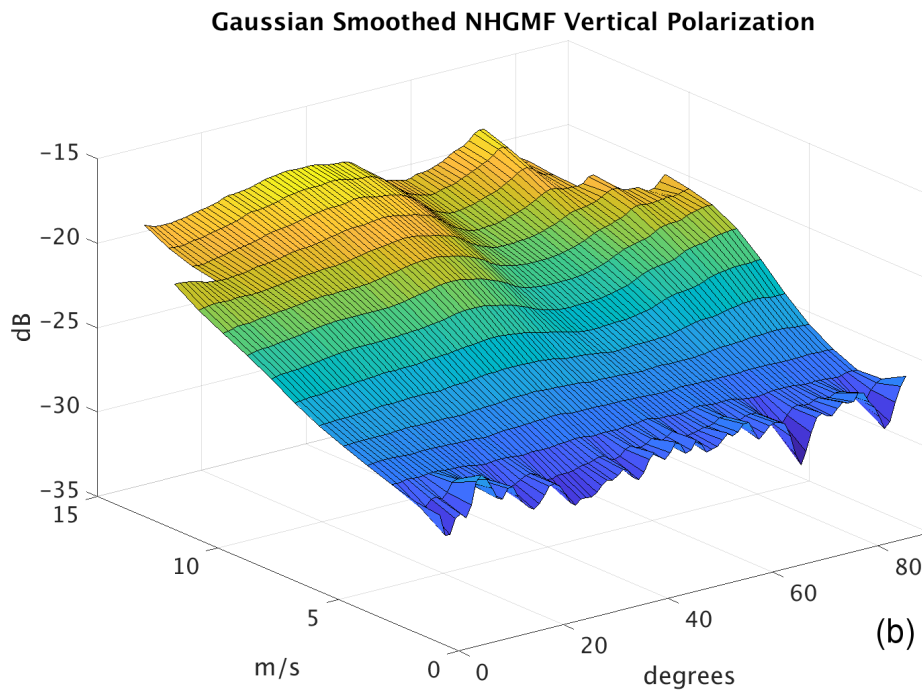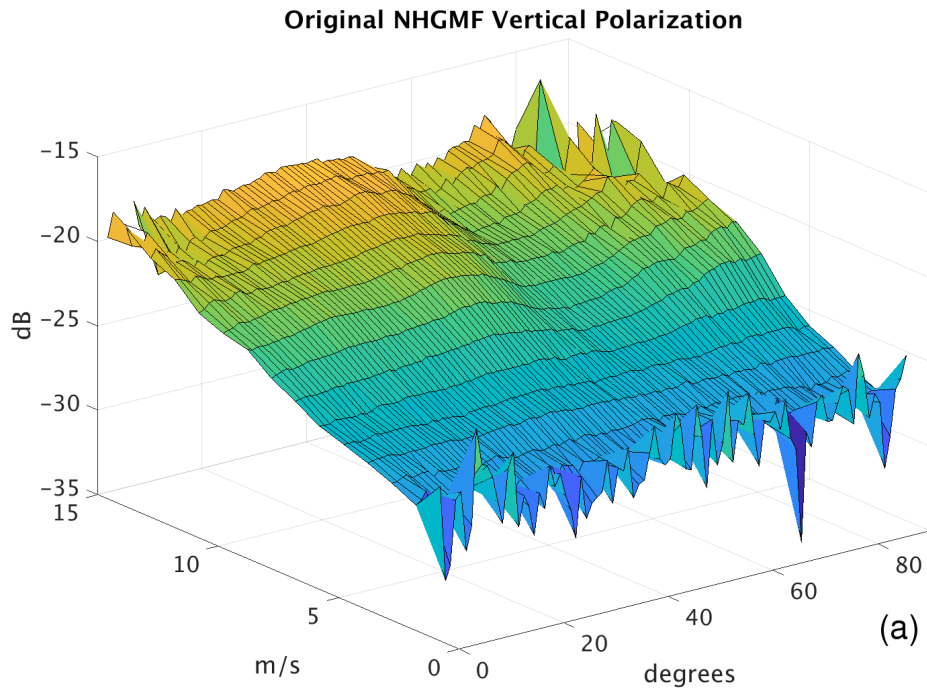
Original NHGMF Vertical Polarization

Gaussian Smoothed NHGMF Vertical Polarization

Figure A.1: (a) shows the noisy NHGMF for the vertical polarization. (b) shows (a) smoothed with a gaussian filter. The QuikSCAT measured σ^0 are binned according to HRCM wind directions and speeds.
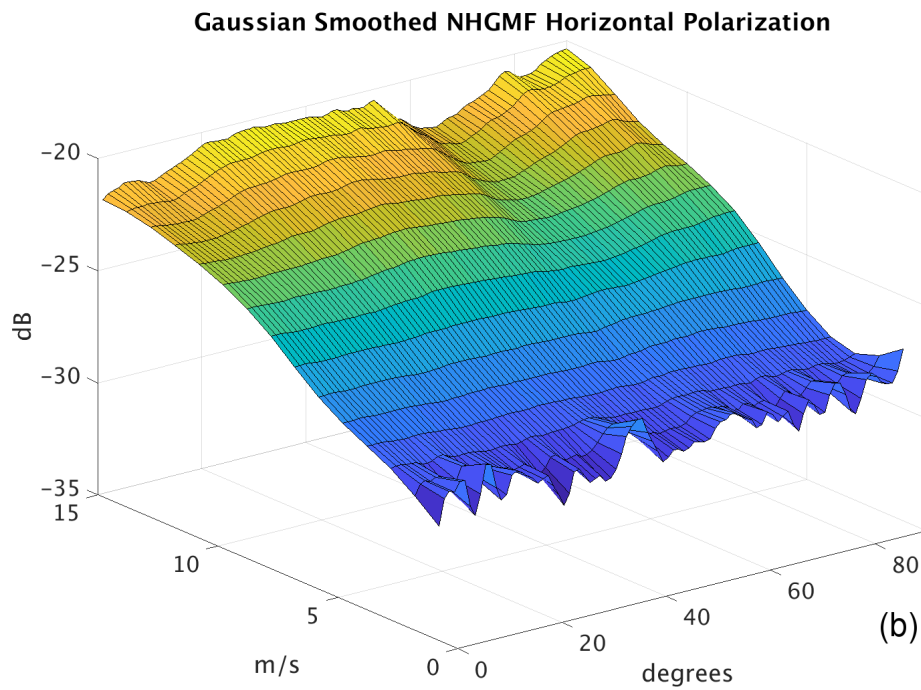
Original NHGMF Horizontal Polarization

(a)

Gaussian Smoothed NHGMF Horizontal Polarization

(b)

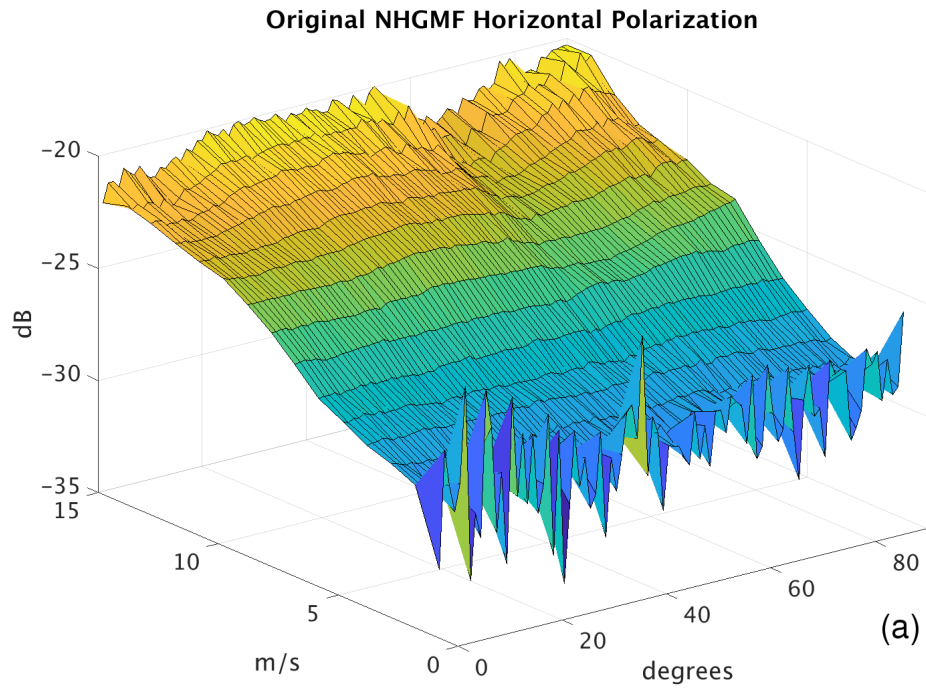Figure A.2: (a) shows the noisy NHGMF for the horizontal polarization. (b) shows (a) smoothed with a gaussian filter. The QuikSCAT measured σ^0 are binned according to HRCM wind directions and speeds.
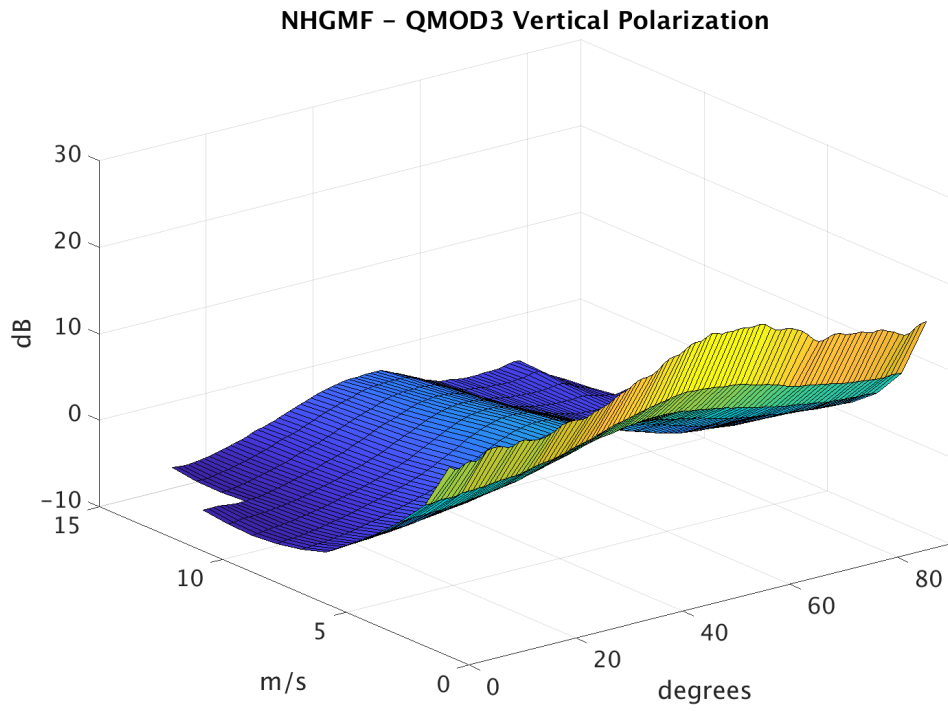
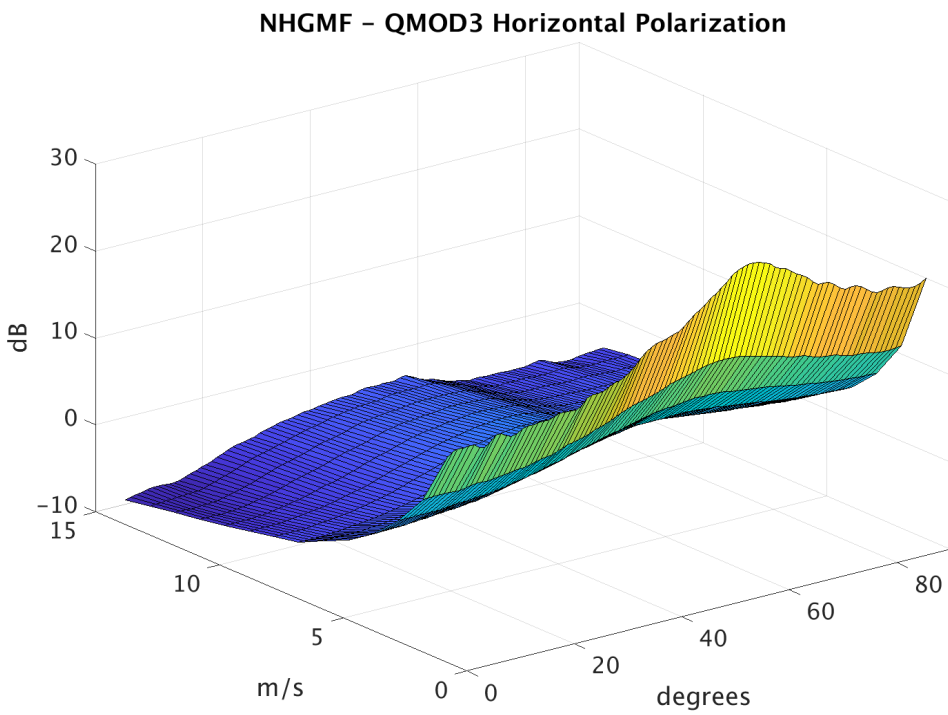Figure A.3: Difference between NHGMF and QMOD3 for the vertical polarization.

Figure A.4: Difference between NHGMF and QMOD3 for the horizontal polarization.